A finite volume WENO scheme for immiscible inviscid two-phase flows

Zhe Li, G. Oger, David Le Touzé

HAL Id: hal-02869797

https://hal.science/hal-02869797

Submitted on 15 Jun 2022

A finite volume WENO scheme for immiscible inviscid two-phase flows

Zhe Li*, Guillaume Oger, David Le Touzé

ᵃEcole Centrale Nantes, LHEEA Research Department (ECN and CNRS), Nantes, France

Abstract

This article presents a two-phase finite volume (FV) method based on the concept of equilibrium volume fraction for simulating inviscid two-phase flows. A reduced three-equation hyperbolic system is adopted as the governing equations, which is closed with a barotropic equation of state for both phases. A modified weighted essentially non-oscillatory (WENO) scheme is proposed for reconstructing the fluid state at cell-interfaces, which can avoid strictly pressure or velocity oscillations near material interfaces in the test-case of the advection of an isolated interface, while retaining the convergence order of the WENO scheme in 1D and 2D cases. Besides, with the generalized Riemann invariants (GRI), the eigenstructure of the hyperbolic system is analyzed and an approximate Riemann flux solver is proposed based on the linearization of the GRI. The semi-discrete system is explicitly integrated in time by means of the classical 4th-order Runge-Kutta (RK4) scheme. The proposed scheme is validated in a series of two-phase test-cases, such as advection of a two-phase vortex, linear sloshing, long-time wave propagation and dam-break flows, for which good agreements are obtained with the references.

Keywords: Two-phase finite volume method, WENO reconstruction, approximate Riemann flux solver, free-surface flows, oscillation-free

1. Introduction

Multiphase flows are widely present in nature as well as in industrial applications, such as ocean waves, sloshing/impacting problems in a liquid tank and atomization of a fuel jet, etc. This type of fluid flows is usually immiscible and of high density ratios between the two phases, which makes it challenging for computational fluid dynamics (CFD) methods to handle high density ratios and to maintain sharp phase-interfaces in a relatively efficient way.

Given these physical characteristics of two-phase flows, it is of primary importance to choose an appropriate mathematical model to describe the necessary physics, which is expected to be mathematically well-posed and easy to solve using a numerical scheme. Insightful reviews on the mathematical models for two-phase flows

---

*Corresponding author
Email address:* `zhe.li@ec-nantes.fr` (Zhe Li)

can be found in [9, 26, 33]. In the present work, we adopt a weakly-compressible two-phase model based on a hyperbolic system of three equations, which are the mass conservation equation for both phases and the momentum conservation equation for the two-phase mixture, closed with a barotropic equation of state (EOS). Notice that, although without energy equation, this reduced three-equation system is sufficient for representing the physics in the targeted weakly-compressible two-phase flows, in which the physical compressibility is not of interest. Thus, highly-compressible multiphase flows, such as strong shock waves, are not considered in the scope of the present work. Initially tested by Chanteperdrix [6], this model has been recently applied by Grenier et al. [16] for simulating two-phase free-surface flows with an implicit low-Mach scheme. In this two-phase model, it is assumed that both phases have the same velocity and the pressure equilibrium is instantaneously accomplished, i.e. at any given location the pressure of the two phases are always the same. As stated by Drew [9], this instantaneous pressure equilibrium is an adequate assumption for the fluid flows where the speed of sound in each phase is large compared with velocities of interest, which is the case in the present work for weakly-compressible flows. More importantly, it can be proven that the adopted 'single-pressure & single-velocity' model is a well-posed hyperbolic system [33], hence it has less mathematical difficulties to solve using a numerical scheme. Recently, this assumption has also been applied in a general formulation for various types of multiphase flows [29]. Here it is worth noting that surface tension and viscosity effects are not considered in the present paper and will be studied in the future work. The reason for this choice is that without physical surface tension and viscous terms in the governing equations, it is straightforward to assess the properties such as the stability and the numerical dissipation of the proposed scheme.

In the present work, we consider to apply a high-order (≥ 3) scheme in order to have a good compromise between the CPU time and precision [5]. To do so, we propose a finite volume (FV) formulation based on a 5th-order weighted essentially non-oscillatory (WENO) scheme for simulating weakly-compressible two-phase flows. Initially proposed by Liu et al. [22], WENO schemes [30] have been widely adopted for capturing discontinuities with appropriate stencils and for attaining desired high order accuracies in smooth regions. Promising results have been obtained in several recent works [7, 12, 17, 19, 31, 28, 32, 41], in which WENO schemes were used for handling high-Mach compressible multiphase flows in the presence of the interaction between phase interfaces and shock waves. One of the difficulties in these types of numerical simulations is that pressure oscillations may occur near the phase interface, which are not only non-physical (purely numerical error) but also may cause numerical instabilities. Indeed, as stated by Abgrall et al. [1, 2], it is generally a major difficulty for a multiphase numerical scheme to avoid this type of pressure oscillations, even in the case of the advection of an isolated material interface with uniform pressure and velocity fields, which is named as 'the Abgrall test-case' hereafter in the present paper.

In 2006, Johnsen and Colonius [19] have proposed a FV-WENO scheme which can avoid pressure oscillations

near the material interface in the Abgrall test-case, by reconstructing the primitive variables instead of the conservative variables in the WENO reconstruction step. The desired formal convergence order of WENO scheme (3rd- and 5th-orders) have been obtained in a 1D test-case. In 2014, Coralic and Colonius [7] have shown that, despite of the advantage of oscillation-free feature, if one directly reconstructs the primitive variables [19], the convergence order of the WENO scheme is limited to 2nd-order in a 2D vortex advection test-case. In order to avoid pressure oscillations near material interfaces and to retain the convergence order of the WENO scheme simultaneously, Coralic and Colonius [7] proposed a reconstruction procedure, summarized as: (i) first-time WENO reconstruction of the conservative variables to obtain the primitive variables at the Gauss quadrature points within each FV-cell; (ii) Gauss quadrature to have the cell-average values of the primitive variables; (iii) second-time WENO reconstruction of the primitive variables to get the fluid state at each cell-interface. Notice that, in the dimension-by-dimension fashion [34], each WENO reconstruction requires twice 'sweeps' in 2D cases in each direction in order to get the interpolated values at cell-interfaces. Thanks to this reconstruction procedure, they succeeded in obtaining a 5th-order convergence in a 2D vortex advection test-case.

Here we propose a FV-WENO scheme which can avoid pressure oscillations and retain the convergence order, using only once the WENO reconstruction. First, we choose to reconstruct the conservative variables in order to retain the convergence order of the WENO scheme. Second, we summarize two necessary conditions for ensuring the oscillation-free feature of a numerical scheme in the Abgrall test-case

- *Condition-I*: Given uniform (constant in space) velocity and pressure fields, the velocity and pressure reconstructed by means of the WENO scheme at cell-interfaces should remain constant;

- *Condition-II*: With the numerical flux computed by an approximate Riemann flux solver, the velocity and pressure fields at next instant (updated using an time integration scheme) should remain constant in space.

One may notice that it is easy to satisfy *Condition-I* when using the primitive variables (pressure and velocity) in the reconstruction step. However, this choice will degrade the convergence order of WENO schemes down to 2nd-order in multi-dimensional cases, as shown in [7]. In the present work, we propose a modified WENO scheme satisfying *Condition-I* by means of: (i) the use of a common smoothness indicator for the conservative variables $\tilde{\rho}_1$ and $\tilde{\rho}_2$; (ii) the reconstruction of the mixture density ρ for deriving the velocity at cell-interfaces. The main advantages of the proposed scheme are its relatively simple algorithmics and small computational efforts it requires. Nevertheless, the proposed numerical framework cannot be directly applied to simulate violent and challenging cases involving significant volume changes, which is hence out of the scope of the present paper. In addition, inspired of the works of Tokareva and Toro [35, 36], we utilize the generalized Riemann invariants (GRI) [37] to provide an analysis on the mathematical property of the adopted three-equation hyperbolic system and

3

then propose a linearized two-phase Riemann flux solver based on the GRI. Furthermore, the classical 4th-order Runge-Kutta scheme is applied to integrate in time the semi-discrete system of equations in an explicit way. It is shown that the proposed linearized Riemann flux solver and the 4th-order Runge-Kutta time integrator satisfy *Condition-II*, i.e. the constant velocity and pressure fields are retained at next instant. As a consequence, the proposed FV-WENO scheme satisfies the above two conditions, which means that the oscillation-free feature is ensured. It is here worth noting that, as did in [7, 34], two Gauss quadrature points are used for the surface integral of flux at cell-interfaces. Despite the lower theoretical accuracy order that could be expected, we have observed a 5th-order convergence of the proposed scheme in the advection of a multiphase vortex test-case, which is consistent with the results presented in [7, 34].

The rest of the paper is organized as follows. Section 2 presents the adopted three-equation mathematical model for describing weakly-compressible two-phase flows with a barotropic closure law. The finite volume formulation is briefly presented in Section 3. In Section 4, the reason of pressure oscillations in the present numerical framework is firstly given, followed by the proposed modifications to the WENO reconstruction scheme. Based on the GRI, a linearized Riemann flux solver is presented in Section 5. A short discussion on the stability issues and some limiters is given in Section 6. The proposed FV-WENO scheme is validated using a series of numerical test-cases in the presence of two-phase free-surface flows, which are shown in Section 7. Finally, the conclusions are drawn in Section 8.

2. Mathematical models

2.1. A three-equation model for weakly-compressible two-phase flows

In the present work, we adopt a three-equation model [6, 16] for describing weakly-compressible inviscid two-phase fluid flows. The system of governing equations consists of the mass conservation equation for the two phases and the momentum conservation equation for the mixture, given as

$$
\begin{cases}
\dfrac{\partial \tilde{\rho}_1}{\partial t} + \nabla \cdot (\tilde{\rho}_1 \mathbf{u}) = 0, \\[2mm]
\dfrac{\partial \tilde{\rho}_2}{\partial t} + \nabla \cdot (\tilde{\rho}_2 \mathbf{u}) = 0, \\[2mm]
\dfrac{\partial (\rho \mathbf{u})}{\partial t} + \nabla \cdot (\rho \mathbf{u} \otimes \mathbf{u} + p\mathbf{I}) = \rho \mathbf{g},
\end{cases}
\tag{1}
$$

where $\tilde{\rho}_k(\mathbf{x},t) = \alpha_k(\mathbf{x},t)\rho_k(\mathbf{x},t)$ with $\alpha_k(\mathbf{x},t)$ and $\rho_k(\mathbf{x},t)$ being respectively the volume fraction and density of the kth phase ($k = 1,2$) at the location $\mathbf{x}$ and time t. By definition, one has $\sum_k \alpha_k(\mathbf{x},t) = \alpha_1(\mathbf{x},t) + \alpha_2(\mathbf{x},t) = 1$. In addition, $\mathbf{u}(\mathbf{x},t)$ denotes the velocity of the mixture, which is shared by both of the two phases, as shown in Equation (1). The density and pressure of the mixture are defined as $\rho(\mathbf{x},t) = \sum_k \alpha_k(\mathbf{x},t)\rho_k(\mathbf{x},t)$ and $p(\mathbf{x},t) = \sum_k \alpha_k(\mathbf{x},t)p_k(\mathbf{x},t)$, respectively. $p_k(\mathbf{x},t)$ denotes the individual pressure of the kth phase, which is

related to $\rho_k(\mathbf{x}, t)$ by means of the chosen equation of state (EOS) discussed subsequently. $\mathbf{I}$ is the identity matrix and $\mathbf{g}$ is the body force per unit mass.

Moreover, the instantaneous pressure equilibrium assumption is adopted, which means that the individual pressures of the two phases are always the same, i.e. $p(\mathbf{x}, t) = p_1(\mathbf{x}, t) = p_2(\mathbf{x}, t), \forall \mathbf{x} \in \Omega_f, \forall t \in [0, +\infty)$. As commented by Drew [9], this assumption is adequate for the cases where the speed of sound is sufficiently large compared to the velocity of interest, or in other words, the Ma number is sufficiently small, which is the case for weakly-compressible fluid flows. As a result, the present system of governing equations can be categorized as a 'single-pressure & single-velocity' two-phase model [33], which is hyperbolic with the adopted EOS, as shown subsequently.

2.2. Barotropic closure law

The individual pressure p_k is related to each density ρ_k by means of an EOS. As did in [16], we adopt a barotropic EOS in order to close the system of equations (1), which is given as

$$p_k = p_0 + c_k^2(\rho_k - \rho_{k,0}), \tag{2}$$

where p_0, $\rho_{k,0}$ and c_k are three constants denoting the reference pressure, the reference density and the speed of sound for the kth phase, respectively, with $k = 1, 2$. This barotropic EOS can be adopted as no thermal effects are considered in the present work, since there is no energy or temperature equation in the system of governing equations (1).

More importantly, with this barotropic closure law, the adopted three-equation two-phase model is a hyperbolic system possessing real eigenvalues, which are related to the speed of propagation of information (the speed of sound) in the fluid domain.

2.3. Speed of sound in the two-phase mixture

In the present weakly-compressible multiphase model, the speed of sound in the two-phase mixture, noted as $c(\mathbf{x}, t)$, can be expressed as

$$c = \frac{1}{\sqrt{\rho \left(\dfrac{\alpha_1}{\rho_1 c_1^2} + \dfrac{\alpha_2}{\rho_2 c_2^2} \right)}}, \tag{3}$$

of which the derivation is provided in Appendix A. As an example, Figure 1 shows the evolution of the speed of sound in an air-water mixture, as the volume fraction of water α_1 varies from 0 to 1. One may observe that when the volume fraction $\alpha_1(\mathbf{x}, t)$ is close to 0.5, the local speed of sound in the mixture can be much smaller than any of the two individual speeds of sound c_1 and c_2. Similar features of the speed of sound in the mixture for other multiphase models have been reported in [21, 24, 29, 33]. This phenomenon has also been observed experimentally by Costigan and Whalley [8] in their measurements of speed of sound in air-water flows.
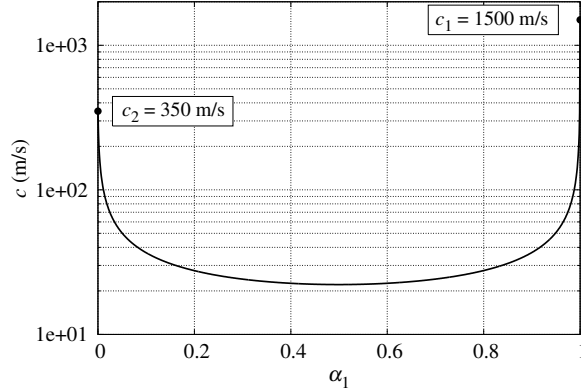
Figure 1: Speed of sound in an air-water mixture with $\rho_1 = 1000$ kg/m^3, $\rho_2 = 1$ kg/m^3, $c_1 = 1500$ m/s and $c_2 = 350$ m/s.

2.4. Equilibrium volume fraction

As shown in Equation (1), there is no advection equation for the volume fraction field $\alpha_k(\mathbf{x}, t)$ in the system of governing equations. This means that no extra equation is needed to update the volume fraction at each new instant. As performed in [16], given $\tilde{\rho}_1$ and $\tilde{\rho}_2$, we can determine the volume fraction α_1 so that the pressure equilibrium condition is ensured, by solving the following equation

$$p_0 + c_1^2 \left(\frac{\tilde{\rho}_1}{\alpha_1} - \rho_{1,0} \right) = p_0 + c_2^2 \left(\frac{\tilde{\rho}_2}{1 - \alpha_1} - \rho_{2,0} \right). \tag{4}$$

Once α_1 is obtained, the volume fraction of the second phase is computed by $\alpha_2 = 1 - \alpha_1$. It is then easy to prove that with positive $\tilde{\rho}_1$ and $\tilde{\rho}_2$, there exists a unique valid equilibrium volume fraction α_1 by solving Equation (4). As did in [6], let us rewrite Equation (4) as

$$\tilde{\rho}_2 c_2^2 \gamma^2 - (q - \tilde{q})\gamma - \tilde{\rho}_1 c_1^2 = 0, \tag{5}$$

where $\gamma = \alpha_1/(1 - \alpha_1)$, $q = \rho_{2,0} c_2^2 - \rho_{1,0} c_1^2$ and $\tilde{q} = \tilde{\rho}_2 c_2^2 - \tilde{\rho}_1 c_1^2$. Given $\tilde{\rho}_1 > 0$ and $\tilde{\rho}_2 > 0$, this quadratic equation (5) possesses two real solutions

$$\begin{cases} \gamma^+ = \dfrac{q - \tilde{q} + \sqrt{(q - \tilde{q})^2 + 4\tilde{\rho}_2 c_2^2 \tilde{\rho}_1 c_1^2}}{2\tilde{\rho}_2 c_2^2} > 0, \\ \gamma^- = \dfrac{q - \tilde{q} - \sqrt{(q - \tilde{q})^2 + 4\tilde{\rho}_2 c_2^2 \tilde{\rho}_1 c_1^2}}{2\tilde{\rho}_2 c_2^2} < 0, \end{cases} \tag{6}$$

of which γ^+ is the unique valid solution, since α_1 must satisfy the condition $0 < \alpha_1 < 1$. Finally, the unique equilibrium volume fraction is obtained as $\alpha_1 = \gamma^+/(1 + \gamma^+)$.

3. Finite volume formulation

In the present work, the finite volume method is adopted to solve the governing equations (1). The fluid domain Ω_f is discretized into a finite number of fixed control volumes, i.e. $\Omega_f = \sum_e \Omega_e$, so that Equation (1) can be rewritten in the following integral form for each control volume Ω_e

$$\frac{\mathrm{d}}{\mathrm{d}t} \int_{\Omega_e} \mathbf{U}\,\mathrm{d}\Omega + \int_{\Gamma_e} \mathbf{K}\mathbf{n}\,\mathrm{d}\Gamma = \int_{\Omega_e} \mathbf{S}\,\mathrm{d}\Omega, \tag{7}$$

where $\mathbf{U}$, $\mathbf{K}$, $\mathbf{n}$ and $\mathbf{S}$ denote respectively the vector of conservative variables, the flux matrix, the outward normal vector on the surface Γ_e of Ω_e and the vector of source term, given as

$$\mathbf{U} = \begin{bmatrix} \tilde{\rho}_1 \\ \tilde{\rho}_2 \\ \rho u \\ \rho v \end{bmatrix}, \ \mathbf{K} = \begin{bmatrix} \mathbf{F} & \mathbf{G} \end{bmatrix} = \begin{bmatrix} \tilde{\rho}_1 u & \tilde{\rho}_1 v \\ \tilde{\rho}_2 u & \tilde{\rho}_2 v \\ \rho uu + p & \rho uv \\ \rho vu & \rho vv + p \end{bmatrix}, \ \mathbf{n} = \begin{bmatrix} n_x \\ n_y \end{bmatrix} \text{ and } \mathbf{S} = \begin{bmatrix} 0 \\ 0 \\ \rho g_x \\ \rho g_y \end{bmatrix}. \tag{8}$$

In addition, $\mathbf{F}$ and $\mathbf{G}$ denote the flux vectors in the x and y directions respectively. Equation (8) is expressed here in 2D but its extension to 3D is straightforward.

In a fixed Cartesian mesh, Equation (7) can be written for the mesh cell over $[x_{i-1/2}, x_{i+1/2}] \times [y_{j-1/2}, y_{j+1/2}]$ as follows

$$\begin{aligned}
\frac{\mathrm{d}\overline{\mathbf{U}}_{i,j}}{\mathrm{d}t} = &-\frac{1}{\Delta x \Delta y} \left(\int_{y_{j-1/2}}^{y_{j+1/2}} \mathbf{F}(x_{i+1/2}, y, t)\,\mathrm{d}y - \int_{y_{j-1/2}}^{y_{j+1/2}} \mathbf{F}(x_{i-1/2}, y, t)\,\mathrm{d}y \right) \\
&-\frac{1}{\Delta x \Delta y} \left(\int_{x_{i-1/2}}^{x_{i+1/2}} \mathbf{G}(x, y_{j+1/2}, t)\,\mathrm{d}x - \int_{x_{i-1/2}}^{x_{i+1/2}} \mathbf{G}(x, y_{j-1/2}, t)\,\mathrm{d}x \right) + \overline{\mathbf{S}}_{i,j},
\end{aligned} \tag{9}$$

where $\overline{\mathbf{U}}_{i,j} = \overline{\mathbf{U}}_{i,j}(t)$ and $\overline{\mathbf{S}}_{i,j} = \overline{\mathbf{S}}_{i,j}(t)$ denote respectively the cell-average values of the conservative variables and the source term, defined as

$$\begin{cases}
\overline{\mathbf{U}}_{i,j}(t) = \dfrac{1}{\Delta x \Delta y} \displaystyle\int_{y_{j-1/2}}^{y_{j+1/2}} \int_{x_{i-1/2}}^{x_{i+1/2}} \mathbf{U}(x, y, t)\,\mathrm{d}x\,\mathrm{d}y, \\[4mm]
\overline{\mathbf{S}}_{i,j}(t) = \dfrac{1}{\Delta x \Delta y} \displaystyle\int_{y_{j-1/2}}^{y_{j+1/2}} \int_{x_{i-1/2}}^{x_{i+1/2}} \mathbf{S}(x, y, t)\,\mathrm{d}x\,\mathrm{d}y,
\end{cases} \tag{10}$$

with $\Delta x = x_{i+1/2} - x_{i-1/2}$ and $\Delta y = y_{j+1/2} - y_{j-1/2}$ being the cell spacing in x- and y-directions, respectively.

Before carrying out the time integration of Equation (9), one needs to evaluate the surface integrals on the right hand side. As suggested in [7, 34], a two-point Gauss quadrature rule is utilized to compute the surface

integral of flux at each cell boundary, for example

$$\int\limits_{y_{j-1/2}}^{y_{j+1/2}} \mathbf{F}(x_{i+1/2}, y, t)\, \mathrm{d}y \simeq \sum_\sigma w_\sigma \mathbf{F}(x_{i+1/2}, y_\sigma, t), \tag{11}$$

where $w_\sigma = \Delta y/2$ denotes the quadrature weight for the σth-Gauss point at $y_\sigma = y_j \pm \Delta y/(2\sqrt{3})$ and the flux function is evaluated with an approximate Riemann flux solver, i.e. $\mathbf{F}(x_{i+1/2}, y_\sigma, t) \simeq \hat{\mathbf{F}}(\mathbf{U}_\sigma^{\mathrm{L}}, \mathbf{U}_\sigma^{\mathrm{R}})$ with $\mathbf{U}_\sigma^{\mathrm{L}}$ and $\mathbf{U}_\sigma^{\mathrm{R}}$ being the reconstructed states by WENO scheme at the left and right sides of the cell-interface.

In the present work, we apply the classical 4th-order Runge-Kutta time integrator to Equation (9) in order to update the cell-average state to the next instant, i.e. from $\overline{\mathbf{U}}_{i,j}^{n} = \overline{\mathbf{U}}_{i,j}(t^n)$ to $\overline{\mathbf{U}}_{i,j}^{n+1} = \overline{\mathbf{U}}_{i,j}(t^{n+1})$. Because of the explicit feature of the scheme, the time-step Δt is chosen as [5]

$$\Delta t = \mathrm{CFL}\frac{\min\limits_{e}\left(\Delta x, \Delta y\right)}{\max\limits_{e}\left(|\mathbf{u}| + c\right)}, \tag{12}$$

where the CFL number is set equal to 0.7 in all the numerical test-cases presented in the following. As an explicit weakly-compressible scheme [40], the present method has a certain number of advantages, such as there is no need to solve a Poisson equation, it is easy to implement and it usually maintains good scaling properties, although the time-step is restricted because of the explicit feature.

4. WENO reconstruction scheme

As mentioned previously, the WENO reconstruction scheme is used to interpolate the variables at each cell-interface with high-order accuracy. In this section, the WENO reconstruction step of the proposed multiphase scheme, which satisfies *Condition-I* given in Introduction, will be presented with details.

4.1. Reconstructed variables

At the beginning of each time-step, the only available data are the newly updated cell-average values of the conservative variables which are obtained by means of the time integration. Hence, it is straightforward to reconstruct the conservative variables at each cell-interface using the cell-average states within the stencils.

For example, in 1D cases with uniform mesh spacing, let $\phi(x)$ be any one of the conservative variables $\tilde{\rho}_1$, $\tilde{\rho}_2$ and ρu, the 5th-order accurate reconstructed values of $\phi(x)$ on the left side of the cell-interface at $x_{i+1/2}^{\mathrm{L}}$ can be expressed as

$$[\phi]_{i+1/2}^{\mathrm{L}} = \frac{\omega_0}{6}\left(2\overline{\phi}_{i-2} - 7\overline{\phi}_{i-1} + 11\overline{\phi}_i\right) + \frac{\omega_1}{6}\left(-\overline{\phi}_{i-1} + 5\overline{\phi}_i + 2\overline{\phi}_{i+1}\right) + \frac{\omega_2}{6}\left(2\overline{\phi}_i + 5\overline{\phi}_{i+1} - \overline{\phi}_{i+2}\right), \tag{13}$$

where ω_l denotes the weighting coefficient for the lth-stencil ($l = 0, 1, 2$) and $\omega_l = d_l$ when there is no WENO smoothness effect with d_l being the ideal weighting coefficient which are equal to $d_0 = 1/10$, $d_1 = 3/5$ and

$d_2 = 3/10$ for $[\phi]^{\mathrm{L}}_{i+1/2}$. Moreover, we note hereafter $[\bullet]^{\times}_{\triangle}$ as the WENO reconstruction operator that gives the interpolated value of the variable '$\bullet$' on the '$\times$' side of the cell-interface at the position '$\triangle$'.

Now, we shall demonstrate that, when there is no WENO smoothness effect, i.e. $\omega_l = d_l$, the reconstructed state at the cell-interface satisfies *Condition-I*.

To do so, let us take the left side of the cell-interface at $x^{\mathrm{L}}_{i+1/2}$ as an example. Using the formula given in Equation (13), the reconstructed variables $\tilde{\rho}_1 = \alpha_1 \rho_1$ and $\tilde{\rho}_2 = \alpha_2 \rho_2$ can be obtained and rewritten as

$$\begin{cases} [\tilde{\rho}_1]^{\mathrm{L}}_{i+1/2} = \sum_m \zeta_m \overline{(\alpha_1 \rho_1)}_m, \\ [\tilde{\rho}_2]^{\mathrm{L}}_{i+1/2} = \sum_m \zeta_m \overline{(\alpha_2 \rho_2)}_m, \end{cases} \tag{14}$$

where ζ_m denotes the coefficient for the mth-cell-average value $\overline{(\alpha_k \rho_k)}_m$ within the three stencils with $m = i-2, i-1, i, i+1, i+2$. With the condition $\omega_l = d_l$, one can have $\zeta_{i-2} = d_0/3 = 1/30$, $\zeta_{i-1} = -7d_0/6 - d_1/6 = -13/60$, $\zeta_i = 11d_0/6 + 5d_1/6 + d_2/3 = 47/60$, $\zeta_{i+1} = d_1/3 + 5d_2/6 = 9/20$ and $\zeta_{i+2} = -d_2/6 = -1/20$. Note here that, since there is no smoothness effect, ζ_m is entirely determined by the mesh spacing and is the same for obtaining $[\tilde{\rho}_1]^{\mathrm{L}}_{i+1/2}$ and $[\tilde{\rho}_2]^{\mathrm{L}}_{i+1/2}$.

Given a uniform pressure field, e.g. $p(x,t) = p_0$, $\forall x \in \Omega_f$ at the current instant t, one has $\rho_1 = \rho_{1,0}$ and $\rho_2 = \rho_{2,0}$, hence

$$\begin{cases} [\tilde{\rho}_1]^{\mathrm{L}}_{i+1/2} = \sum_m \zeta_m \overline{(\alpha_1)}_m \rho_{1,0}, \\ [\tilde{\rho}_2]^{\mathrm{L}}_{i+1/2} = \sum_m \zeta_m \overline{(\alpha_2)}_m \rho_{2,0}. \end{cases} \tag{15}$$

These reconstructed values $[\tilde{\rho}_1]^{\mathrm{L}}_{i+1/2}$ and $[\tilde{\rho}_2]^{\mathrm{L}}_{i+1/2}$ are then used to get the equilibrium volume fraction $\alpha^{\mathrm{L}}_{1,i+1/2}$ at the cell-interface by solving Equation (4) as follows

$$c_1^2 \left(\frac{[\tilde{\rho}_1]^{\mathrm{L}}_{i+1/2}}{\alpha^{\mathrm{L}}_{1,i+1/2}} - \rho_{1,0} \right) = c_2^2 \left(\frac{[\tilde{\rho}_2]^{\mathrm{L}}_{i+1/2}}{1 - \alpha^{\mathrm{L}}_{1,i+1/2}} - \rho_{2,0} \right), \tag{16}$$

which, with the help of Equation (15) and $\overline{(\alpha_2)}_m = 1 - \overline{(\alpha_1)}_m$, can be written as

$$c_1^2 \left(\frac{\rho_{1,0} \sum_m \zeta_m \overline{(\alpha_1)}_m}{\alpha^{\mathrm{L}}_{1,i+1/2}} - \rho_{1,0} \right) = c_2^2 \left(\frac{\rho_{2,0} - \rho_{2,0} \sum_m \zeta_m \overline{(\alpha_1)}_m}{1 - \alpha^{\mathrm{L}}_{1,i+1/2}} - \rho_{2,0} \right), \tag{17}$$

of which one obvious solution is

$$\alpha^{\mathrm{L}}_{1,i+1/2} = \sum_m \zeta_m \overline{(\alpha_1)}_m. \tag{18}$$

Since it is previously shown that there is a *unique* valid solution, Equation (18) is just the sought solution for the equilibrium volume fraction on the left side of the cell-interface at $x^{\mathrm{L}}_{i+1/2}$. It can then be easily verified that the pressure at the cell-interface is equal to the constant value, i.e. $p^{\mathrm{L}}_{i+1/2} = p_0$.

9

Similarly, in order to evaluate the velocity $u^{\mathrm{L}}_{i+1/2}$ at $x^{\mathrm{L}}_{i+1/2}$, one needs to firstly get the reconstructed conservative variable ρu as

$$[\rho u]^{\mathrm{L}}_{i+1/2} = \sum_m \zeta_m \overline{(\rho u)}_m, \tag{19}$$

which gives the velocity at the cell-interface as

$$u^{\mathrm{L}}_{i+1/2} = \frac{[\rho u]^{\mathrm{L}}_{i+1/2}}{\rho^{\mathrm{L}}_{i+1/2}} = \frac{[\rho u]^{\mathrm{L}}_{i+1/2}}{[\tilde{\rho}_1]^{\mathrm{L}}_{i+1/2} + [\tilde{\rho}_2]^{\mathrm{L}}_{i+1/2}} = \frac{\sum\limits_m \zeta_m \overline{(\rho u)}_m}{\sum\limits_m \zeta_m \overline{(\alpha_1 \rho_1)}_m + \sum\limits_m \zeta_m \overline{(\alpha_2 \rho_2)}_m} = \frac{\sum\limits_m \zeta_m \overline{(\rho u)}_m}{\sum\limits_m \zeta_m \overline{(\rho)}_m}. \tag{20}$$

Given a uniform velocity field, e.g. $u(x,t) = u_0, \forall x \in \Omega_f$, the velocity at the cell-interface is then evaluated as

$$u^{\mathrm{L}}_{i+1/2} = \frac{u_0 \sum\limits_m \zeta_m \overline{(\rho)}_m}{\sum\limits_m \zeta_m \overline{(\rho)}_m} = u_0. \tag{21}$$

As a consequence, in the absence of smoothness effect, given uniform pressure and velocity fields, the original WENO reconstruction scheme satisfies *Condition-I*, which means that it can ensure that the reconstructed pressure and velocity at each cell-interface have constant values. Similarly, one can obtain the same conclusion for $p^{\mathrm{R}}_{i-1/2}$ and $u^{\mathrm{R}}_{i-1/2}$.

4.2. Smoothness effect

The idea of WENO reconstruction scheme is to assign a weighting coefficient for each stencil, based on its smoothness, such that the reconstruction essentially utilizes the information from the relatively smooth stencils. Using a well defined smoothness indicator, a WENO scheme based on three stencils can retain a 5th-order accuracy in smooth areas of the domain, while being able to provide a lower order reconstructed value at the locations where there exists a strong discontinuity. In the present work, we adopt the widely used WENO smoothness indicators given by Jiang and Shu [18], defined as

$$\beta_l = \int\limits_{x_{i-1/2}}^{x_{i+1/2}} \Delta x \left(\frac{\partial \mathcal{P}_l}{\partial x} \right)^2 + \Delta x^3 \left(\frac{\partial^2 \mathcal{P}_l}{\partial x^2} \right)^2 \, \mathrm{d}x, \tag{22}$$

where β_l and $\mathcal{P}_l$ denote the smoothness measurement and the local 2nd-order polynomial for the lth-stencil. For $l = 0, 1$ and 2, one has

$$\begin{cases} \beta_0 = \dfrac{13}{12} \left(\overline{\phi}_{i-2} - 2\overline{\phi}_{i-1} + \overline{\phi}_i \right)^2 + \dfrac{1}{4} \left(\overline{\phi}_{i-2} - 4\overline{\phi}_{i-1} + 3\overline{\phi}_i \right)^2, \\ \beta_1 = \dfrac{13}{12} \left(\overline{\phi}_{i-1} - 2\overline{\phi}_i + \overline{\phi}_{i+1} \right)^2 + \dfrac{1}{4} \left(\overline{\phi}_{i-1} - \overline{\phi}_{i+1} \right)^2, \\ \beta_2 = \dfrac{13}{12} \left(\overline{\phi}_i - 2\overline{\phi}_{i+1} + \overline{\phi}_{i+2} \right)^2 + \dfrac{1}{4} \left(3\overline{\phi}_i - 4\overline{\phi}_{i+1} + \overline{\phi}_{i+2} \right)^2, \end{cases} \tag{23}$$

10

with which the weight ω_l is then obtained applying

$$\omega_l = \frac{\xi_l}{\xi_0 + \xi_1 + \xi_2} \text{ , with } \xi_l = \frac{d_l}{(\beta_l + \varepsilon)^2}, \tag{24}$$

where ε is a small enough value in case of $\beta_l = 0$, which is set as $\varepsilon = 10^{-6}$ as suggested by Jiang and Shu [18]. It is worth noting here that the smoothness indicators β_l in Equation (23) are not dimensionless. Hence using the same value of ε for all the variables, i.e. $\tilde{\rho}_1$, $\tilde{\rho}_2$ and ρu, may generate some problems for choosing the appropriate stencils [14]. In the present work, we propose to renormalize β_l with a characteristic quantity ϕ_0^2 for each variable, in such a way that the weight is now computed by

$$\omega_l = \frac{\breve{\xi}_l}{\breve{\xi}_0 + \breve{\xi}_1 + \breve{\xi}_2} \text{ , with } \breve{\xi}_l = \frac{d_l}{\left(\breve{\beta}_l + \varepsilon\right)^2} \text{ , and } \breve{\beta}_l = \frac{\beta_l}{\phi_0^2}, \tag{25}$$

where $\phi_0 = \rho_{1,0}, \rho_{2,0}$ and $\rho_{1,0} u_0$ for the reconstructed variables $\tilde{\rho}_1$, $\tilde{\rho}_2$ and ρu, respectively.

Using the weighting coefficient given in Equation (25) for the WENO reconstruction scheme (13), one can avoid utilizing the information from the stencils containing strong discontinuities. However, as shown in the following, such WENO scheme cannot ensure *Condition-I*, when considering the smoothness effect.

As mentioned previously, each reconstructed variable possesses its own WENO smoothness indicator β_l, e.g. let us assign $\breve{\beta}_{1,l}$ for $\tilde{\rho}_1$ and $\breve{\beta}_{2,l}$ for $\tilde{\rho}_2$. Because $\breve{\beta}_{1,l}$ and $\breve{\beta}_{2,l}$ are generally not identical, although they are indeed related via the volume fraction field, the weight are generally not the same, i.e. $\omega_{1,l} \neq \omega_{2,l}$. Given a uniform pressure field ($p = p_0$), the reconstructed $\tilde{\rho}_1$ and $\tilde{\rho}_2$ at the cell-interface can then be expressed as

$$\begin{cases} [\tilde{\rho}_1]_{i+1/2}^{\mathrm{L}} = \sum_m \zeta_{1,m} \overline{(\alpha_1)}_m \rho_{1,0}, \\ [\tilde{\rho}_2]_{i+1/2}^{\mathrm{L}} = \sum_m \zeta_{2,m} \overline{(\alpha_2)}_m \rho_{2,0}, \end{cases} \tag{26}$$

where one should note that $\zeta_{1,m} \neq \zeta_{2,m}$ in the general case.

To obtain the volume fraction $\alpha_{1,i+1/2}^{\mathrm{L}}$, $[\tilde{\rho}_1]_{i+1/2}^{\mathrm{L}}$ and $[\tilde{\rho}_2]_{i+1/2}^{\mathrm{L}}$ given by Equation (26) are then substituted in Equation (16), which gives

$$c_1^2 \left(\frac{\rho_{1,0} \sum_m \zeta_{m,1} \overline{(\alpha_1)}_m}{\alpha_{1,i+1/2}^{\mathrm{L}}} - \rho_{1,0} \right) = c_2^2 \left(\frac{\rho_{2,0} - \rho_{2,0} \sum_m \zeta_{m,2} \overline{(\alpha_1)}_m}{1 - \alpha_{1,i+1/2}^{\mathrm{L}}} - \rho_{2,0} \right), \tag{27}$$

of which the solution $\alpha_{1,i+1/2}^{\mathrm{L}}$ is generally not equal to $\sum_m \zeta_{1,m} \overline{(\alpha_1)}_m$ or $\sum_m \zeta_{2,m} \overline{(\alpha_1)}_m$, since $\zeta_{1,m} \neq \zeta_{2,m}$. Hence the pressure at the cell-interface $x_{i+1/2}^{\mathrm{L}}$ is not equal to the constant value, i.e. $p_{i+1/2}^{\mathrm{L}} \neq p_0$. As a consequence, a pressure oscillation may occur from this cell-interface.

Besides, given a uniform velocity field ($u = u_0$), the interface velocity $u_{i+1/2}^{\mathrm{L}}$ is obtained with Equation (20)

as

$$u_{i+1/2}^{\mathrm{L}} = \frac{u_0 \sum\limits_m \zeta_{\rho,m} \overline{(\rho)}_m}{\sum\limits_m \zeta_{1,m} \overline{(\alpha_1 \rho_1)}_m + \sum\limits_m \zeta_{2,m} \overline{(\alpha_1 \rho_1)}_m}, \tag{28}$$

where $\zeta_{\rho,m}$ denotes the coefficient related to the smoothness of the mixture density field $\rho(x,t)$. Obviously, one may observe that $u_{i+1/2}^{\mathrm{L}} \neq u_0$, because the coefficients $\zeta_{\rho,m}$, $\zeta_{1,m}$ and $\zeta_{2,m}$ are generally not the same.

4.3. WENO smoothness indicators in the proposed method

With the previous analysis on the smoothness effects, in the present work, we propose a modified WENO reconstruction scheme, which is based on

(i) *Common smoothness indicator for $\tilde{\rho}_1$ and $\tilde{\rho}_2$.* As shown previously, the pressure oscillation is basically due to the fact the $\breve{\beta}_{1,l}$ is generally not equal to $\breve{\beta}_{2,l}$. Hence, we propose a common dimensionless smoothness indicator $\breve{\beta}_{c,l}$, computed as

$$\breve{\beta}_{c,l} = \sqrt{\breve{\beta}_{1,l} \breve{\beta}_{2,l}}, \tag{29}$$

which is a reasonable choice, because $\breve{\beta}_{c,l}$ embodies the smoothness in both $\tilde{\rho}_1$ and $\tilde{\rho}_2$ fields which are correlated through the volume fraction α_1, especially when the two densities ρ_1 and ρ_2 vary little under the weakly-compressible hypothesis. Using this common smoothness indicator $\breve{\beta}_{c,l}$, the coefficients $\zeta_{1,m}$ and $\zeta_{2,m}$ in Equation (27) become identical, i.e. $\zeta_{1,m} = \zeta_{2,m}$, which gives a unique solution of $\alpha_{1,i+1/2}^{\mathrm{L}}$ that verifies $p_{i+1/2}^{\mathrm{L}} = p_0$.

(ii) *Reconstruction of the mixture density ρ.* In order to avoid the velocity oscillation, we propose to reconstruct the mixture density at the cell-interface $x_{i+1/2}^{\mathrm{L}}$, instead of using the sum of $[\tilde{\rho}_1]_{i+1/2}^{\mathrm{L}}$ and $[\tilde{\rho}_2]_{i+1/2}^{\mathrm{L}}$, which is then used to get the velocity $u_{i+1/2}^{\mathrm{L}}$ at the cell-interface as

$$u_{i+1/2}^{\mathrm{L}} = \frac{[\rho u]_{i+1/2}^{\mathrm{L}}}{[\rho]_{i+1/2}^{\mathrm{L}}} = \frac{u_0 \sum\limits_m \zeta_{\rho,m} \overline{(\rho)}_m}{\sum\limits_m \zeta_{\rho,m} \overline{(\rho)}_m} = u_0, \tag{30}$$

which means that the velocity at the cell-interface has the constant value u_0. Notice that two candidates for the value of the mixture density $\rho_{i+1/2}^{\mathrm{L}}$ at the cell-interface are available, which are $[\rho]_{i+1/2}^{\mathrm{L}}$ and $[\tilde{\rho}_1]_{i+1/2}^{\mathrm{L}} + [\tilde{\rho}_2]_{i+1/2}^{\mathrm{L}}$. In smooth regions, the difference between these two values is of order $\mathcal{O}(\Delta x^5)$. In order to ensure a strict oscillation-free property, it is suggested to use $[\rho]_{i+1/2}^{\mathrm{L}}$ exclusively for evaluating the velocity at the cell-interface.

Once again, the same conclusion can be obtained for $p_{i+1/2}^{\mathrm{R}}$ and $u_{i+1/2}^{\mathrm{R}}$. Consequently, with the above two modifications (i) and (ii), the proposed WENO scheme can satisfy *Condition-I*. The influence on the convergence order is discussed with details subsequently.

12

4.4. Convergence order

One of the advantages of the WENO scheme is that the numerical solver can choose the relatively smooth stencils, based on the smoothness indicators, by means of a unified formula for the whole computational domain. Hence, the smoothness effect should not degrade the high convergence order in smooth areas. As shown in the following, the proposed WENO scheme can retain the original convergence order in smooth areas.

As demonstrated by Jiang and Shu [18], the 5th-order convergence of WENO scheme can be retained, if

$$\omega_l = d_l + \mathcal{O}\left(\Delta x^2\right), \tag{31}$$

where ω_l is given in Equation (25) and d_l is the optimal weight. To satisfy Equation (31), it suffices to have

$$\breve{\beta}_l = D\left(1 + \mathcal{O}\left(\Delta x^2\right)\right), \tag{32}$$

where $\breve{\beta}_l$ denotes the smoothness indicator given in Equation (25) and D is a non-zero quantity independent of l.

Equation (32) can be easily verified with a Taylor expansion of Equation (23). However, Taylor expansion cannot be directly carried out, since $\overline{\phi}_i$ denotes the cell-average value of the function ϕ, but not the value of ϕ at x_i. Nevertheless, one can assume there exists a function $\varphi(x)$, such that

$$\varphi_i = \varphi(x_i) = \frac{1}{\Delta x} \int\limits_{x_i - 1/2\Delta x}^{x_i + 1/2\Delta x} \phi(x)\,\mathrm{d}x = \overline{\phi}_i, \tag{33}$$

with which the Taylor expansion for $\breve{\beta}_0$, $\breve{\beta}_1$ and $\breve{\beta}_2$ can be carried out at x_i as

$$\begin{cases} \breve{\beta}_0 = \dfrac{1}{\phi_0^2}\varphi_i'^2\Delta x^2 + \dfrac{1}{\phi_0^2}\left(\dfrac{13}{12}\varphi_i''^2 - \dfrac{2}{3}\varphi_i'\varphi_i'''\right)\Delta x^4 - \dfrac{1}{\phi_0^2}\left(\dfrac{13}{6}\varphi_i''\varphi_i''' - \dfrac{1}{2}\varphi_i'\varphi_i''''\right)\Delta x^5 + \mathcal{O}\left(\Delta x^6\right), \\[2mm] \breve{\beta}_1 = \dfrac{1}{\phi_0^2}\varphi_i'^2\Delta x^2 + \dfrac{1}{\phi_0^2}\left(\dfrac{13}{12}\varphi_i''^2 + \dfrac{1}{3}\varphi_i'\varphi_i'''\right)\Delta x^4 + \mathcal{O}\left(\Delta x^6\right), \\[2mm] \breve{\beta}_2 = \dfrac{1}{\phi_0^2}\varphi_i'^2\Delta x^2 + \dfrac{1}{\phi_0^2}\left(\dfrac{13}{12}\varphi_i''^2 - \dfrac{2}{3}\varphi_i'\varphi_i'''\right)\Delta x^4 + \dfrac{1}{\phi_0^2}\left(\dfrac{13}{6}\varphi_i''\varphi_i''' - \dfrac{1}{2}\varphi_i'\varphi_i''''\right)\Delta x^5 + \mathcal{O}\left(\Delta x^6\right). \end{cases} \tag{34}$$

Obviously, dividing the smoothness indicator β_l by ϕ_0^2 still allows one to express $\breve{\beta}_l$ in the form as shown in Equation (32), which means this renormalization does not degrade the convergence order of the WENO scheme. Now it is necessary to assess whether the common smoothness indicator $\breve{\beta}_{c,l}$ can retain the convergence order.

To do so, let us express the smoothness indicators $\breve{\beta}_{1,l}$ and $\breve{\beta}_{2,l}$ for the variables $\tilde{\rho}_1$ and $\tilde{\rho}_2$, respectively, as

$$\begin{cases} \breve{\beta}_{1,l} = D_1\left(1 + \mathcal{O}\left(\Delta x^2\right)\right), \\ \breve{\beta}_{2,l} = D_2\left(1 + \mathcal{O}\left(\Delta x^2\right)\right), \end{cases} \tag{35}$$

where D_1 and D_2 are two quantities independent of l. Hence, the common smoothness indicator $\breve{\beta}_{c,l}$ can then be expressed as

$$\breve{\beta}_{c,l} = \sqrt{\breve{\beta}_{1,l}\breve{\beta}_{2,l}} = \sqrt{D_1 D_2 \left(1 + \mathcal{O}\left(\Delta x^2\right)\right)}, \tag{36}$$

which, by means of a Taylor expansion analysis, can be rewritten as

$$\breve{\beta}_{c,l} = D_c \left(1 + \mathcal{O}\left(\Delta x^2\right)\right), \text{ with } D_c = \sqrt{D_1 D_2}, \tag{37}$$

which means that the common dimensionless smoothness indicator $\breve{\beta}_{c,l}$ proposed in Equation (29) satisfies the sufficient condition (32).

Hence, in the proposed WENO scheme, all the variables can be reconstructed at the cell-interface with 5th-order accuracy, i.e. $[\phi]^{\text{L}}_{i+1/2} = \phi(x_{i+1/2}) + \mathcal{O}(\Delta x^5)$, where $\phi = \tilde{\rho}_1, \tilde{\rho}_2, \rho, \rho u, \rho v$. Furthermore, the proposed scheme can avoid oscillations when given uniform pressure and velocity fields in an efficient way, compared with the strategy proposed in [7] requiring twice the WENO reconstructions.

5. Approximate Riemann flux solver

Given the reconstructed variables $\mathbf{U}^{\text{L}}_\sigma$ and $\mathbf{U}^{\text{R}}_\sigma$ at both sides of each cell-interface, a numerical flux solver $\hat{\mathbf{F}}(\mathbf{U}^{\text{L}}_\sigma, \mathbf{U}^{\text{R}}_\sigma)$ is then utilized to evaluate the flux $\mathbf{F}$ at the cell-interface, as shown in Equation (11). In the present work, we propose a linearized Riemann flux solver, based on the generalized Riemann invariants.

5.1. Eigenstructure of the hyperbolic system

To estimate the flux at cell-interface in the x-direction, one usually analyzes the quasi-linear x-split governing equations expressed as

$$\frac{\partial \mathbf{W}}{\partial t} + \mathbf{A}\frac{\partial \mathbf{W}}{\partial x} = \mathbf{0}, \tag{38}$$

where $\mathbf{W} = [\tilde{\rho}_1, \tilde{\rho}_2, u, v]^\top$. In addition, the matrix $\mathbf{A}$ is given as

$$\mathbf{A} = \begin{bmatrix} u & 0 & \tilde{\rho}_1 & 0 \\ 0 & u & \tilde{\rho}_2 & 0 \\ \dfrac{\tilde{c}_1^2}{\rho} & \dfrac{\tilde{c}_2^2}{\rho} & u & 0 \\ 0 & 0 & 0 & u \end{bmatrix}, \text{ with } \begin{cases} \tilde{c}_1 = \dfrac{\partial p}{\partial \tilde{\rho}_1}, \\ \tilde{c}_2 = \dfrac{\partial p}{\partial \tilde{\rho}_2}, \end{cases} \tag{39}$$

so that the pressure gradient has been expressed as

$$\frac{\partial p}{\partial x} = \frac{\partial p}{\partial \tilde{\rho}_1}\frac{\partial \tilde{\rho}_1}{\partial x} + \frac{\partial p}{\partial \tilde{\rho}_2}\frac{\partial \tilde{\rho}_2}{\partial x} = \tilde{c}_1^2\frac{\partial \tilde{\rho}_1}{\partial x} + \tilde{c}_2^2\frac{\partial \tilde{\rho}_2}{\partial x}. \tag{40}$$

The matrix $\mathbf{A}$ possesses the following eigenvalues

$$\begin{cases} \lambda_1 = u - c, \\ \lambda_2 = \lambda_3 = u, \\ \lambda_4 = u + c, \end{cases} \tag{41}$$

where c denotes the speed of sound in the two-phase mixture, computed as

$$c = \sqrt{\frac{\tilde{\rho}_1 \tilde{c}_1^2 + \tilde{\rho}_2 \tilde{c}_2^2}{\rho}}, \tag{42}$$

which is equivalent to Equation (3), as shown in Appendix A. As the individual density ρ_k and the volume fraction α_k are positive in Equation (3), c has a real value, so do the eigenvalues. Consequently, the present three-equation two-phase model is a hyperbolic system, of which the corresponding right eigenvectors are given as

$$\mathbf{r}_1 = \begin{bmatrix} \tilde{\rho}_1 \\ \tilde{\rho}_2 \\ -c \\ 0 \end{bmatrix}, \ \mathbf{r}_2 = \begin{bmatrix} \tilde{c}_2^2 \\ -\tilde{c}_1^2 \\ 0 \\ 0 \end{bmatrix}, \ \mathbf{r}_3 = \begin{bmatrix} 0 \\ 0 \\ 0 \\ 1 \end{bmatrix} \text{ and } \mathbf{r}_4 = \begin{bmatrix} \tilde{\rho}_1 \\ \tilde{\rho}_2 \\ c \\ 0 \end{bmatrix}. \tag{43}$$

5.2. Generalized Riemann invariants

Based on the simple wave theory [20], the generalized Riemann invariants (GRI) condition [13, 37] states the fact that an invariant relation holds across each eigenvalue-related wave in the x-t plane, as shown in Figure 2. For the present hyperbolic system, λ_1 and λ_4 are related respectively to two genuinely non-linear waves, and λ_2 and λ_3 are both related to a contact wave which is linearly degenerated. In the recent works of Tokareva and Toro [35, 36], the GRI condition has been successfully applied to solve the Baer-Nunziato equations [3] for compressible flows.
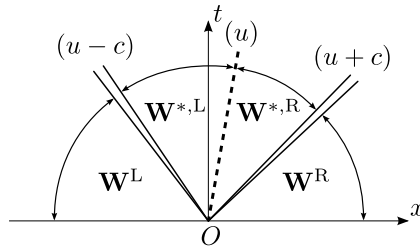

Figure 2: Wave structure of the present hyperbolic system.

Across the λ_a-related wave, the variation $\mathrm{d}\mathbf{W}_a$ is parallel to the corresponding right eigenvector $\mathbf{r}_a$ in the phase space, which gives

15

- across the λ_1-related wave:

$$\frac{d\tilde{\rho}_1}{\tilde{\rho}_1} = \frac{d\tilde{\rho}_2}{\tilde{\rho}_2} = \frac{du}{-c} = \frac{dv}{0}, \text{ hence } \begin{cases} \tilde{\rho}_1 \, du + c \, d\tilde{\rho}_1 = 0, \\ \tilde{\rho}_2 \, du + c \, d\tilde{\rho}_2 = 0, \\ dv = 0, \end{cases} \tag{44}$$

- across the λ_4-related wave:

$$\frac{d\tilde{\rho}_1}{\tilde{\rho}_1} = \frac{d\tilde{\rho}_2}{\tilde{\rho}_2} = \frac{du}{c} = \frac{dv}{0}, \text{ hence } \begin{cases} \tilde{\rho}_1 \, du - c \, d\tilde{\rho}_1 = 0, \\ \tilde{\rho}_2 \, du - c \, d\tilde{\rho}_2 = 0, \\ dv = 0, \end{cases} \tag{45}$$

- across the λ_2- and λ_3-related wave (contact wave):

$$\frac{d\tilde{\rho}_1}{\tilde{c}_2^2} = \frac{d\tilde{\rho}_2}{-\tilde{c}_1^2} = \frac{du}{0} = \frac{dv}{0} \text{ and } \frac{d\tilde{\rho}_1}{0} = \frac{d\tilde{\rho}_2}{0} = \frac{du}{0} = \frac{dv}{1}, \text{ hence } \begin{cases} \tilde{c}_1^2 \, d\tilde{\rho}_1 + \tilde{c}_2^2 \, d\tilde{\rho}_2 = 0, \\ du = 0. \end{cases} \tag{46}$$

By analyzing the GRI conditions (44), (45) and (46), we summarize several properties of the present three-equation two-phase hyperbolic system, given as follows

(i) since $dv = 0$ across the λ_1- and λ_4-related waves, there is no variation of v across these two waves, i.e. $v^{*,\mathrm{L}} = v^{\mathrm{L}}$ and $v^{*,\mathrm{R}} = v^{\mathrm{R}}$;

(ii) the velocity component u is constant in the star region, because across the contact wave, one has $du = 0$ which indicates that $u^{*,\mathrm{L}} = u^{*,\mathrm{R}} = u^*$;

(iii) the pressure p is constant in the star region, because across the contact wave, the variation of the pressure is equal to zero, since

$$dp = \frac{\partial p}{\partial \tilde{\rho}_1} \, d\tilde{\rho}_1 + \frac{\partial p}{\partial \tilde{\rho}_2} \, d\tilde{\rho}_2 = \tilde{c}_1^2 \, d\tilde{\rho}_1 + \tilde{c}_2^2 \, d\tilde{\rho}_2 = 0, \tag{47}$$

which gives $p^{*,\mathrm{L}} = p^{*,\mathrm{R}} = p^*$;

(iv) with the adopted EOS (2) and the property (iii), the density for each phase remains constant across the contact wave, i.e. $\rho_k^{*,\mathrm{L}} = \rho_k^{*,\mathrm{R}} = \rho_k^*$, with $k = 1, 2$.

5.3. Linearized two-phase Riemann flux solver

Based on the GRI conditions, we propose a linearized Riemann flux solver, inspired of the work in [36]. The idea is to linearize the GRI conditions across the λ_1- and λ_4-waves, which are both related to the speed of sound c, in order to obtain an approximate state in the star region of the two-phase Riemann problem at each cell-interface.

Given Equation (44), the variation of pressure across the λ_1-wave can be expressed as

$$
\begin{aligned}
\mathrm{d}p &= \tilde{c}_1^2 \, \mathrm{d}\tilde{\rho}_1 + \tilde{c}_2^2 \, \mathrm{d}\tilde{\rho}_2, \\
&= \tilde{c}_1^2 \left(-\frac{\tilde{\rho}_1}{c} \, \mathrm{d}u \right) + \tilde{c}_2^2 \left(-\frac{\tilde{\rho}_2}{c} \, \mathrm{d}u \right), \\
&= -\frac{\tilde{\rho}_1 \tilde{c}_1^2 + \tilde{\rho}_2 \tilde{c}_2^2}{c} \, \mathrm{d}u, \\
&= -\rho c \, \mathrm{d}u.
\end{aligned}
\tag{48}
$$

Similarly, based on Equation (45), across the λ_4-wave, one has $\mathrm{d}p = \rho c \, \mathrm{d}u$. Now, we adopt a linearization step by taking $\rho c \simeq \rho^{\mathrm{L}} c^{\mathrm{L}}$ across the λ_1-wave and $\rho c \simeq \rho^{\mathrm{R}} c^{\mathrm{R}}$ across the λ_4-wave, which gives

$$
\begin{cases}
(p^{\mathrm{L}} - \hat{p}^*) + \rho^{\mathrm{L}} c^{\mathrm{L}} (u^{\mathrm{L}} - \hat{u}^*) = 0, \\
(p^{\mathrm{R}} - \hat{p}^*) - \rho^{\mathrm{R}} c^{\mathrm{R}} (u^{\mathrm{R}} - \hat{u}^*) = 0,
\end{cases}
\tag{49}
$$

where $\hat{p}^*$ and $\hat{u}^*$ denote respectively the approximate values of p^* and u^*, which can then be computed as

$$
\begin{cases}
\hat{p}^* = \dfrac{\rho^{\mathrm{L}} c^{\mathrm{L}} \rho^{\mathrm{R}} c^{\mathrm{R}} (u^{\mathrm{L}} - u^{\mathrm{R}}) + (\rho^{\mathrm{R}} c^{\mathrm{R}} p^{\mathrm{L}} + \rho^{\mathrm{L}} c^{\mathrm{L}} p^{\mathrm{R}})}{\rho^{\mathrm{L}} c^{\mathrm{L}} + \rho^{\mathrm{R}} c^{\mathrm{R}}}, \\
\hat{u}^* = \dfrac{(p^{\mathrm{L}} - p^{\mathrm{R}}) + (\rho^{\mathrm{L}} c^{\mathrm{L}} u^{\mathrm{L}} + \rho^{\mathrm{R}} c^{\mathrm{R}} u^{\mathrm{R}})}{\rho^{\mathrm{L}} c^{\mathrm{L}} + \rho^{\mathrm{R}} c^{\mathrm{R}}}.
\end{cases}
\tag{50}
$$

As shown in the property (iv) given previously, we can get the density for each phase in the star region with the EOS (2), i.e. $\hat{\rho}_k^* = \rho_{k,0} + (\hat{p}^* - p_0)/c_k^2$, with $k = 1, 2$.

Besides, from the GRI conditions (44) and (45), one can obtain

$$
\begin{cases}
\rho \, \mathrm{d}u + c \, \mathrm{d}\rho = 0, \quad \text{across the } \lambda_1\text{-wave}, \\
\rho \, \mathrm{d}u - c \, \mathrm{d}\rho = 0, \quad \text{across the } \lambda_4\text{-wave},
\end{cases}
\tag{51}
$$

which can be linearized, giving

$$
\begin{cases}
\rho^{\mathrm{L}} (\hat{u}^* - u^{\mathrm{L}}) + c^{\mathrm{L}} (\hat{\rho}^{*,\mathrm{L}} - \rho^{\mathrm{L}}) = 0, \\
\rho^{\mathrm{R}} (\hat{u}^* - u^{\mathrm{R}}) - c^{\mathrm{R}} (\hat{\rho}^{*,\mathrm{R}} - \rho^{\mathrm{R}}) = 0,
\end{cases}
\tag{52}
$$

where $\hat{\rho}^{*,\mathrm{L}}$ and $\hat{\rho}^{*,\mathrm{R}}$ denote the approximate density of the mixture at the left and right star region, respectively, which are given as

$$
\begin{cases}
\hat{\rho}^{*,\mathrm{L}} = \rho^{\mathrm{L}} - \dfrac{\rho^{\mathrm{L}}}{c^{\mathrm{L}}} (\hat{u}^* - u^{\mathrm{L}}), \\
\hat{\rho}^{*,\mathrm{R}} = \rho^{\mathrm{R}} + \dfrac{\rho^{\mathrm{R}}}{c^{\mathrm{R}}} (\hat{u}^* - u^{\mathrm{R}}).
\end{cases}
\tag{53}
$$

17

Now, given $\hat{\rho}_k^*$, $\hat{\rho}^{*,L}$ and $\hat{\rho}^{*,R}$, we can obtain the volume fraction in the star region by means of the definition of the density of mixture

$$\begin{cases} \hat{\rho}^{*,L} = \hat{\alpha}_1^{*,L}\hat{\rho}_1^* + (1 - \hat{\alpha}_1^{*,L})\hat{\rho}_2^*, \\ \hat{\rho}^{*,R} = \hat{\alpha}_1^{*,R}\hat{\rho}_1^* + (1 - \hat{\alpha}_1^{*,R})\hat{\rho}_2^*. \end{cases} \tag{54}$$

Finally, we have the approximate states of variables within the whole star region, i.e. $\hat{\mathbf{U}}^{*,L}$ and $\hat{\mathbf{U}}^{*,R}$, which allow us to obtain the numerical flux $\hat{\mathbf{F}}_\sigma$ at the σth-Gauss point as

$$\hat{\mathbf{F}}_\sigma = \begin{cases} \mathbf{F}(\hat{\mathbf{U}}_\sigma^{*,L}), & \text{if } \hat{u}^* \geq 0, \\ \mathbf{F}(\hat{\mathbf{U}}_\sigma^{*,R}), & \text{if } \hat{u}^* < 0, \end{cases} \tag{55}$$

where $\mathbf{F}(\mathbf{U})$ is the flux function given in Equation (8). It is here worth noting that Equation (55) is sufficient for weakly-compressible two-phase flows, because the speed of sound is much greater than the fluid velocity. In case of local hypersonic flow, we need to include another two situations

$$\hat{\mathbf{F}}_\sigma = \begin{cases} \mathbf{F}(\mathbf{U}^L), & \text{if } S^L > 0, \\ \mathbf{F}(\mathbf{U}^R), & \text{if } S^R < 0, \end{cases} \tag{56}$$

where S^L and S^R denote the estimation of the speed of wave related to the eigenvalues $\lambda_1 = u - c$ and $\lambda_4 = u + c$, as shown in Figure 2. In the literature [4, 38], several ways have been proposed for estimating the speeds of waves, e.g. $S^L = \min(u^L - c^L, u^R - c^R)$ and $S^R = \max(u^L + c^L, u^R + c^R)$.

Now, we shall show that the proposed linearized two-phase Riemann flux solver satisfies *Condition-II* given in Introduction, i.e. by means of the present numerical flux and the adopted RK4 time integrator, the velocity and pressure of the updated state at the next instant still remain constant.

To do so, let us recall that the proposed WENO scheme satisfies *Condition-I*, hence one has $p^L = p^R = p_0$ and $u^L = u^R = u_0$ at all the cell-interfaces. By means of Equation (50), one can obtain that $\hat{p}^* = p_0$ and $\hat{u}^* = u_0$, which gives $\hat{\rho}^{*,L} = \rho^L$ and $\hat{\rho}^{*,R} = \rho^R$ with Equation (53). In addition, since $\hat{p}^* = p_0$, one has $\hat{\rho}_1^* = \rho_{1,0}$ and $\hat{\rho}_2^* = \rho_{2,0}$ with the EOS. Consequently, by solving Equation (54), one can have $\hat{\alpha}_1^{*,L} = \alpha_1^L$ and $\hat{\alpha}_1^{*,R} = \alpha_1^R$.

Hence, the numerical flux for the ith-cell at $x_{i-1/2}$ and $x_{i+1/2}$ are computed as (e.g. $u_0 > 0$)

$$\hat{\mathbf{F}}_{i-1/2} = \mathbf{F}(\hat{\mathbf{U}}_{i-1/2}^{*,L}) = \begin{bmatrix} \alpha_{1,i-1/2}^L \rho_{1,0} u_0 \\ \alpha_{2,i-1/2}^L \rho_{2,0} u_0 \\ \rho_{i-1/2}^L u_0^2 + p_0 \end{bmatrix} \text{ and } \hat{\mathbf{F}}_{i+1/2} = \mathbf{F}(\hat{\mathbf{U}}_{i+1/2}^{*,L}) = \begin{bmatrix} \alpha_{1,i+1/2}^L \rho_{1,0} u_0 \\ \alpha_{2,i+1/2}^L \rho_{2,0} u_0 \\ \rho_{i+1/2}^L u_0^2 + p_0 \end{bmatrix}, \tag{57}$$

18

with which the first intermediate state $\overline{\mathbf{U}}_i^{(1)}$ for the RK4 scheme can be obtained as

$$\overline{\mathbf{U}}_i^{(1)} = \begin{bmatrix} \overline{(\alpha_1\rho_1)}_i^{(1)} \\ \overline{(\alpha_2\rho_2)}_i^{(1)} \\ \overline{(\rho u)}_i^{(1)} \end{bmatrix} = \begin{bmatrix} \overline{(\alpha_1\rho_1)}_i^n \\ \overline{(\alpha_2\rho_2)}_i^n \\ \overline{(\rho u)}_i^n \end{bmatrix} - \frac{\Delta t}{2\Delta x} \left(\begin{bmatrix} \alpha_{1,i+1/2}^{\mathrm{L}}\rho_{1,0}u_0 \\ \alpha_{2,i+1/2}^{\mathrm{L}}\rho_{2,0}u_0 \\ \rho_{i+1/2}^{\mathrm{L}}u_0^2 + p_0 \end{bmatrix} - \begin{bmatrix} \alpha_{1,i-1/2}^{\mathrm{L}}\rho_{1,0}u_0 \\ \alpha_{2,i-1/2}^{\mathrm{L}}\rho_{2,0}u_0 \\ \rho_{i-1/2}^{\mathrm{L}}u_0^2 + p_0 \end{bmatrix} \right) = \begin{bmatrix} \overline{(\alpha_1)}_i^{(1)}\rho_{1,0} \\ \overline{(\alpha_2)}_i^{(1)}\rho_{2,0} \\ \overline{(\rho)}_i^{(1)}u_0 \end{bmatrix}, \quad (58)$$

with

$$\begin{cases} \overline{(\alpha_1)}_i^{(1)} = \overline{(\alpha_1)}_i^n - \dfrac{\Delta t}{2\Delta x}\left(\alpha_{1,i+1/2}^{\mathrm{L}} - \alpha_{1,i-1/2}^{\mathrm{L}} \right) u_0, \\[2mm] \overline{(\alpha_2)}_i^{(1)} = \overline{(\alpha_2)}_i^n - \dfrac{\Delta t}{2\Delta x}\left(\alpha_{2,i+1/2}^{\mathrm{L}} - \alpha_{2,i-1/2}^{\mathrm{L}} \right) u_0, \\[2mm] \overline{(\rho)}_i^{(1)} = \overline{(\rho)}_i^n - \dfrac{\Delta t}{2\Delta x}\left(\rho_{i+1/2}^{\mathrm{L}} - \rho_{i-1/2}^{\mathrm{L}} \right) u_0. \end{cases} \quad (59)$$

Equation (58) shows that, after one intermediate time integration, α_1, α_2 and ρ vary in time, while ρ_1, ρ_2 (hence p) and u remain constant for all the cells. It can then be easily proven that all the intermediate states as well as the state at the next time-step $\overline{\mathbf{U}}_i^{n+1}$ have constant pressure and velocity fields. Hence the proposed linearized Riemann flux solver and the adopted time integration scheme satisfy *Condition-II*.

6. Stability and limiters

As presented in Section 2, in order to prove the uniqueness of the solution of the volume fraction, one needs to verify that $\tilde{\rho}_1$ and $\tilde{\rho}_2$ are both positive. Indeed, maintaining the positivity of $\tilde{\rho}_1$ and $\tilde{\rho}_2$ are of great importance in the present scheme, not only because of their physical meaning, but also due to the fact that negative values of $\tilde{\rho}_1$ or $\tilde{\rho}_2$ could not give real eigenvalues, which sometimes leads to ill-posed problems with unphysical instabilities [26]. However, it is well known that the conventional WENO scheme cannot guarantee that the reconstructed values of $\tilde{\rho}_1$ or $\tilde{\rho}_2$ are positive at cell-interfaces. In the literature, there exist several positivity-preserving schemes and limiters [25, 43, 44].

In the present work, for the sake of efficiency, we choose to apply a simple limiter for the reconstructed $\tilde{\rho}_1$ and $\tilde{\rho}_2$ at each Gauss point. For both of the two phases ($k = 1, 2$), if the reconstructed value $[\tilde{\rho}_k]_\sigma^{\mathrm{L}}$ or $[\tilde{\rho}_k]_\sigma^{\mathrm{R}}$ is less than a critical value $0.9\varepsilon_\alpha\rho_{k,0}$, where $\varepsilon_\alpha = 10^{-4}$, then it is set to be the cell-average value $\overline{(\tilde{\rho}_k)}_{i,j}$. Although this operation might theoretically degrade the convergence order, it is observed that in practice this limiter is activated only in areas where there exist strong discontinuities of the volume fraction field α_1. In the two subsequent test-cases, it is shown that this limiter does not affect 5th-order convergence of the present WENO scheme.

Besides, we observe that numerical instabilities may occur in relatively violent two-phase flows, in the presence of solid wall boundaries, such as the dam-break flow. This is because the cells near solid walls have only one available stencil for the WENO reconstruction. Using the stencil selection algorithm based on

the comparison of smoothness, one always takes this stencil for reconstruction, even though it contains huge discontinuities, which is the case for the dam-break flow, especially when the water front impacts on the solid wall at the corner of the tank. Hence, for this type of two-phase flows, we adopt a limiter similar as the one used in [34], which sets the reconstructed value $[\phi]_\sigma^{\mathrm{L}}$ to be the cell-average value $\overline{(\phi)}_{i,j}$, if $\left| [\tilde{\rho}_k]_\sigma^{\mathrm{L}} - \overline{(\tilde{\rho}_k)}_{i,j} \right| > 0.9 \overline{(\tilde{\rho}_k)}_{i,j}$.

7. Numerical results

In the following test-cases, all the two-phase flows have a density ratio of 1000, i.e. $\rho_{1,0}/\rho_{2,0} = 1000$, $k = 1$ for water with $\rho_{1,0} = 1000$ kg/m^3 and $k = 2$ for air with $\rho_{2,0} = 1$ kg/m^3. In addition, as the physical compressibility is not of primary importance in all following test-cases, an artificial speed of sound in each fluid c_k is chosen according to the weakly-compressible hypothesis, by comparing with the characteristic fluid velocity in each test-case, for the sake of numerical efficiency. As presented in Introduction, viscous effects are not considered in the governing equations, hence in the following numerical examples, either there is no viscous term in the analytical solution or the viscosity effects are not dominant in the considered physical problems. Accordingly, the free-slip boundary condition is imposed on solid walls, if there are. This is realized by using a mirrored state, e.g. $\mathbf{U}_\sigma^{\mathrm{R}}$, when computing the numerical flux on the solid wall, which possesses the same densities and tangential component but opposite normal velocity component as the ones of the reconstructed state $\mathbf{U}_\sigma^{\mathrm{L}}$.

7.1. Interface advection

7.1.1. 1D advection

In order to verify numerically the oscillation-free feature of the proposed scheme in the Abgrall test-case, we first consider an 1D interface advection, of which the initial condition is given as

$$\alpha_1(x,0) = \begin{cases} 1 - \varepsilon_\alpha, & \text{if } \dfrac{L}{2} - r_0 < x < \dfrac{L}{2} + r_0, \\ \varepsilon_\alpha, & \text{otherwise}, \end{cases} \tag{60}$$

where $\varepsilon_\alpha = 10^{-4}$, $L = 1$ m denotes the length of the 1D computational domain with $x \in [0, L]$ and $r_0 = L/10$ is the radius of the 1D liquid droplet. In addition, $\rho_1(x,0) = \rho_{1,0} = 1000$ kg/m^3 and $\rho_2(x,0) = \rho_{2,0} = 1$ kg/m^3, so that $p(x,0) = p_0 = 0$ Pa. The speed of sound for both fluids are set as $c_1 = c_2 = 70$ m/s and the whole fluid domain is initialized with a uniform velocity field, i.e. $u(x,0) = u_0 = 1$ m/s. Periodic boundary conditions are imposed at the two extremities, at $x = 0$ and $x = L$.

Figure 3 shows the density fields of the mixture at the initial ($t = 0$ s) and the final ($t = 1$ s) instants of the numerical simulation, obtained with the proposed scheme using 64 uniform cells for spacial discretization. The 1D droplet of water moves from left to right and gets back to its initial position after 1 s. It can be clearly observed that the phase-interface becomes smeared or diffused as time evolves. Figure 4 shows the pressure

20

and velocity oscillations in the numerical results obtained with the present and original WENO schemes. We observe that the present WENO scheme can ensure zero oscillation in the pressure and velocity fields. As for the computational efficiency, we observe that the present WENO scheme is approximately 1.65 times more costly than the original WENO scheme. The extra cost is majorly due to the reconstruction of the mixture's density and the computation of the common WENO smoothness for $\tilde{\rho}_1$ and $\tilde{\rho}_2$.
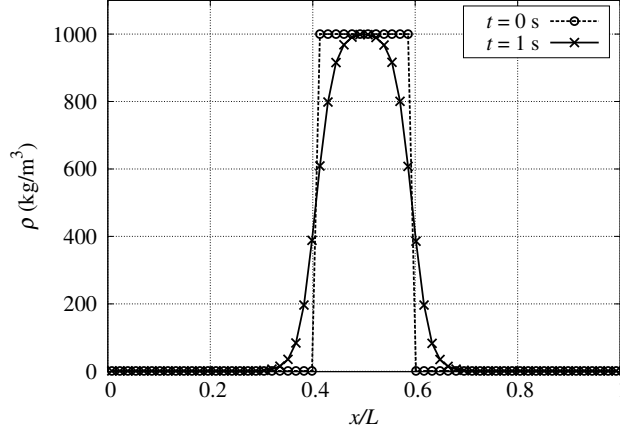
Figure 3: 1D interface advection test-case: density of the mixture at $t = 0$ s and $t = 1$ s.
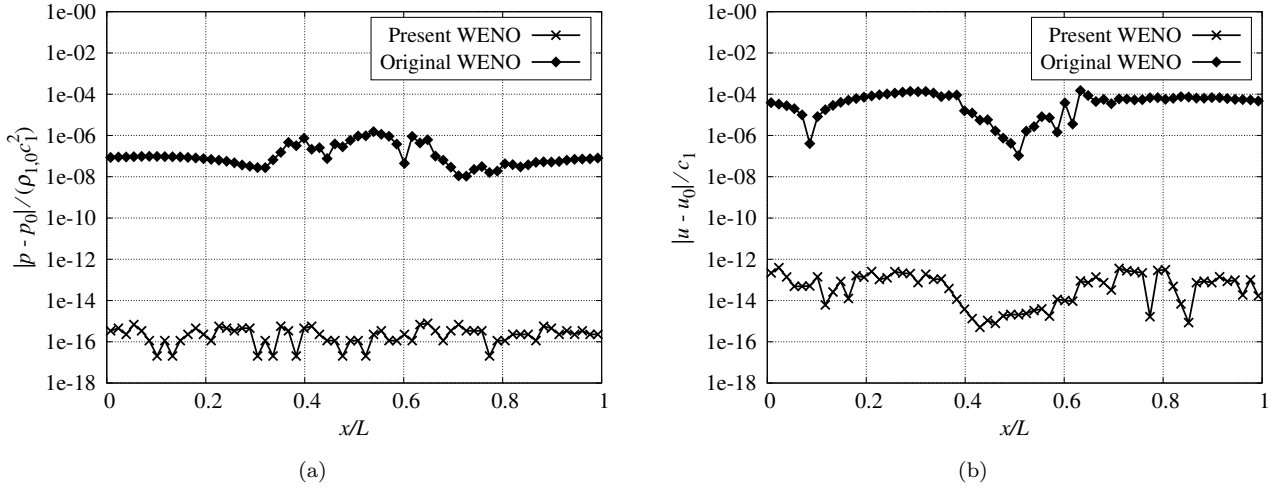
Figure 4: 1D interface advection test-case carried out with the present and original WENO schemes at $t = 1$ s: (a) pressure field; (b) velocity field.

As mentioned in Introduction, the objective of reconstructing conservative variables is to attain high convergence order, i.e. 5th-order in the present work. In order to carry out a convergence study, we initialize the

21

shape of the 1D water droplet with a smoother function

$$\alpha_1(x,0) = (1 - 2\varepsilon_\alpha)\exp\left(-\frac{|x - L/2|^2}{r_0^2}\right) + \varepsilon_\alpha, \tag{61}$$

which is shown in Figure 5-(a). Notice that all the other variables remain the same as in the previous sharp interface advection test-case. The convergence study is carried out using five mesh resolutions with the number of cells $N = 64, 128, 256, 512$ and 1024. The L_1, L_2 and L_∞ errors of the mixture's density at $t = 1$ s are computed as

$$\begin{cases} L_1\text{-Error} = \dfrac{1}{N}\sum_i \dfrac{\left|\overline{\rho}_i^{\text{num}} - \overline{\rho}_i^{\text{ref}}\right|}{\rho_{1,0}}, \\[4mm] L_2\text{-Error} = \sqrt{\dfrac{1}{N}\sum_i \dfrac{\left|\overline{\rho}_i^{\text{num}} - \overline{\rho}_i^{\text{ref}}\right|^2}{\rho_{1,0}^2}}, \\[4mm] L_\infty\text{-Error} = \max_i\left(\dfrac{\left|\overline{\rho}_i^{\text{num}} - \overline{\rho}_i^{\text{ref}}\right|}{\rho_{1,0}}\right), \end{cases} \tag{62}$$

where $\overline{\rho}_i^{\text{num}}$ and $\overline{\rho}_i^{\text{ref}}$ denote respectively the numerical and reference cell-average values of the mixture's density of the ith-cell. Table 1 shows the errors and the convergence orders evaluated by computing

$$\text{Order} = \ln\left(\frac{\text{Error}^q}{\text{Error}^{q+1}}\right)\Big/\ln(2), \tag{63}$$

where Error^q denotes the error corresponding to the qth-mesh resolution. As shown in Table 1 and Figure 5-(b), the present numerical scheme possesses the expected 5th-order convergence in this 1D advection test-case.

Table 1: Numerical errors in the 1D advection test-case.

Number of cells	L_1-Error	L_1-Order	L_2-Error	L_2-Order	L_∞-Error	L_∞-Order
64	8.7542e-4	-	1.5857e-3	-	4.7826e-3	-
128	3.7302e-5	4.5527	6.8293e-5	4.5372	2.1892e-4	4.4493
256	1.2148e-6	4.9405	2.2702e-6	4.9108	8.7785e-6	4.6403
512	3.7243e-8	5.0276	7.1105e-8	4.9967	2.9355e-7	4.9023
1024	1.0935e-9	5.0899	2.1816e-9	5.0265	8.8813e-9	5.0467

7.1.2. 2D advection

Next, we assess the oscillation-free feature of the proposed numerical scheme in a 2D interface advection test-case. The initial volume fraction field α_1 within the $(i,j)^{\text{th}}$-cell is imposed as

$$\alpha_1 = \begin{cases} 1 - \varepsilon_\alpha, & \text{if } (x_{i,j} - x_0)^2 + (y_{i,j} - y_0)^2 < r_0^2, \\ \varepsilon_\alpha, & \text{otherwise,} \end{cases} \tag{64}$$
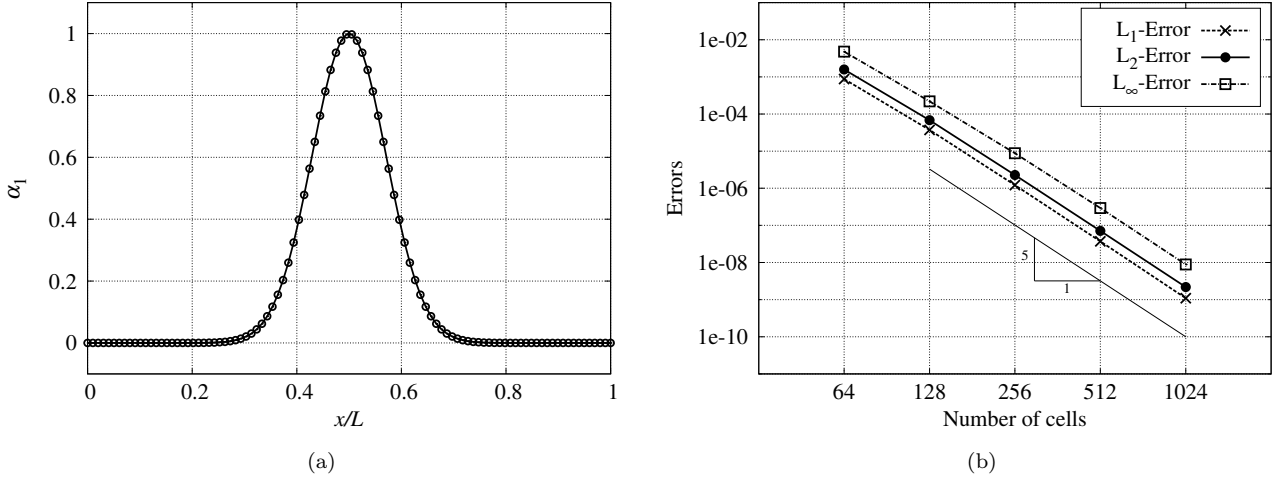
Figure 5: Convergence study in the 1D advection test-case: (a) initial volume fraction field; (b) convergence order.

where $x_{i,j}$ and $y_{i,j}$ denote the coordinates in x- and y- directions of the barycenter of each cell, and x_0 and y_0 the coordinates of the center of the computational domain $[-L, L] \times [-L, L]$ with $L = 1$ m. As in the 1D test-case, periodic conditions are imposed at the four boundaries. The initial uniform velocity and pressure fields are set as $u(x, y, 0) = 2$ m/s, $v(x, y, 0) = 2$ m/s and $p(x, y, 0) = 0$ Pa. The speed of sound is chosen as $c_1 = c_2 = 30$ m/s.

Figure 6 shows the initial and final density fields of the mixture in the simulation using a mesh of size $64\Delta x \times 64\Delta y$. From the pressure field at the final instant as shown in Figure 7, one can observe that a strict zero pressure oscillation is ensured by the proposed scheme in this 2D interface advection test-case, as in the previous 1D advection.

7.2. Multiphase vortex advection

As presented in [7], a numerical scheme possessing a 5th-order convergence property in 1D test-cases might fail to converge with a 5th-order in multi-dimensional cases, such as the one in [19]. Hence, it is necessary to assess the convergence order of the present scheme in 2D where the gradients of all variables have non-zero values. For this purpose, we carry out a convergence study with a 2D multiphase vortex advection test-case, of which the analytical solution is provided in Appendix B.

The initial volume fraction and pressure fields at $t = 0$ s within the periodic computational domain $[-L, L] \times$

23
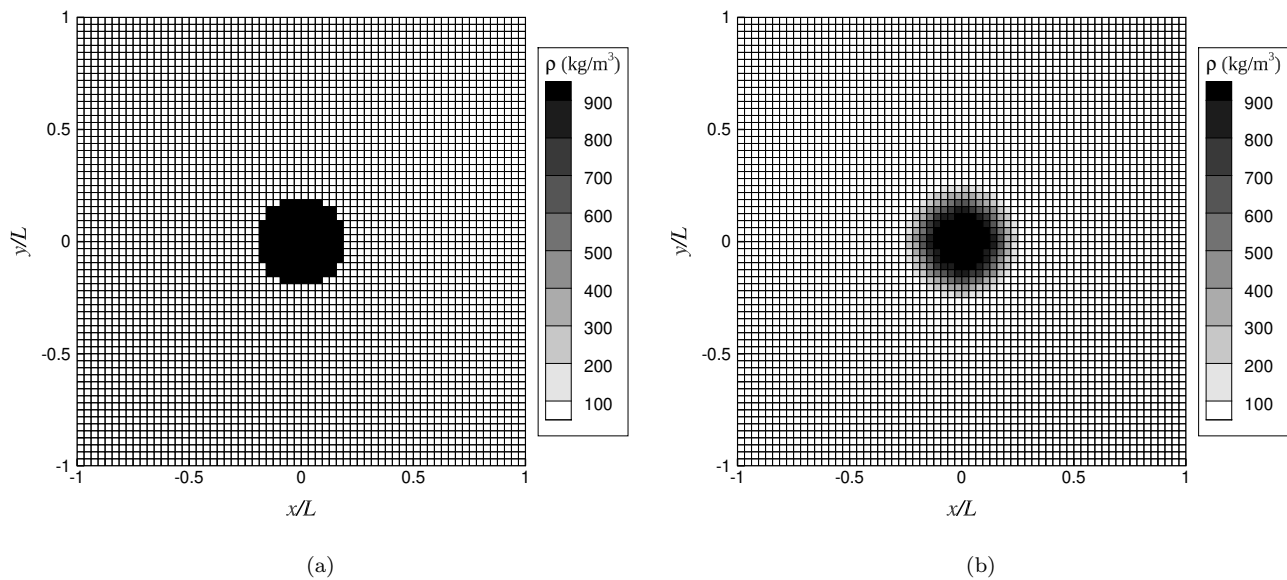
Figure 6: Density fields of the mixture in the 2D interface advection test-case: (a) $t = 0$ s; (b) $t = 1$ s.
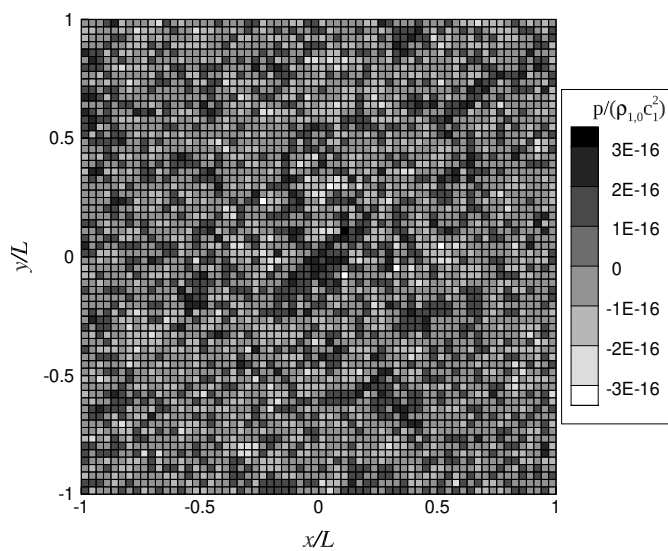
Figure 7: Pressure field at the final instant ($t = 1$ s) in the 2D interface advection test-case.

$[-L, L]$ are imposed as

$$
\begin{cases}
\alpha_1(r, \theta, 0) = (1 - 2\varepsilon_\alpha) \exp\left(-\frac{r^2}{r_0^2}\right) + \varepsilon_\alpha, \\[2mm]
p(r, \theta, 0) = P\left(1 - \exp\left(-\frac{r^2}{r_0^2}\right)\right), \\[2mm]
u(r, \theta, 0) = U - \sin\theta \sqrt{\frac{r}{\rho}\frac{\partial p}{\partial r}}, \\[2mm]
v(r, \theta, 0) = V + \cos\theta \sqrt{\frac{r}{\rho}\frac{\partial p}{\partial r}},
\end{cases}
\tag{65}
$$

where r and θ denote the cylindrical coordinates with $x = r\cos\theta$ and $y = r\sin\theta$, $\varepsilon_\alpha = 10^{-4}$, $r_0 = 0.2L$ with $L = 1$ m, and $P = 0.1\rho_{2,0}c_2^2$ with $c_1 = c_2 = 30$ m/s. The density of both phases ρ_1 and ρ_2 can be obtained with the EOS. Finally, $U = V = 2$ m/s denote the two components of the advection velocity. The initial volume fraction field and the relative velocity vector with respect to the moving frame are shown in Figure 8-(a).

Table 2: Numerical errors in the 2D multiphase vortex advection test-case.

Number of cells	L_1-Error	L_1-Order	L_2-Error	L_2-Order	L_∞-Error	L_∞-Order
64	3.9112e-4	-	1.2847e-3	-	8.8276e-3	-
128	1.9138e-5	4.3531	6.0041e-5	4.4193	4.5100e-4	4.2908
256	6.2019e-7	4.9476	1.9616e-6	4.9358	1.5642e-5	4.8496
512	1.7145e-8	5.1769	5.6494e-8	5.1178	4.6175e-7	5.0822

Table 2 shows the errors and convergence orders of different norms computed using the formulas (62) and (63). In addition, based on these values of errors, the convergence slopes are also given in Figure 8-(b). As expected, a 5th-order convergence is obtained in this 2D multiphase vortex advection test-case using the proposed scheme. Here it is worth noting that, in this convergence study, all physical fields including the volume fraction α_1 should be sufficiently smooth. In the presence of discontinuities, the convergence order will be limited to 1st-order at most.

7.3. Linear sloshing

Now, we consider a 2D linear sloshing test-case [6, 16], of which the configuration is shown in Figure 9. Initially, air and water are both at rest under the gravity effect in a closed tank which is composed of four free-slip solid walls. As $t > 0$, a constant horizontal acceleration a is applied to the whole fluid domain in the positive x-direction, which is equivalent to the case where the tank suddenly moves in the negative x-direction with an acceleration $-a\mathbf{e}_x$. The geometrical and physical parameters are given in Table 3.
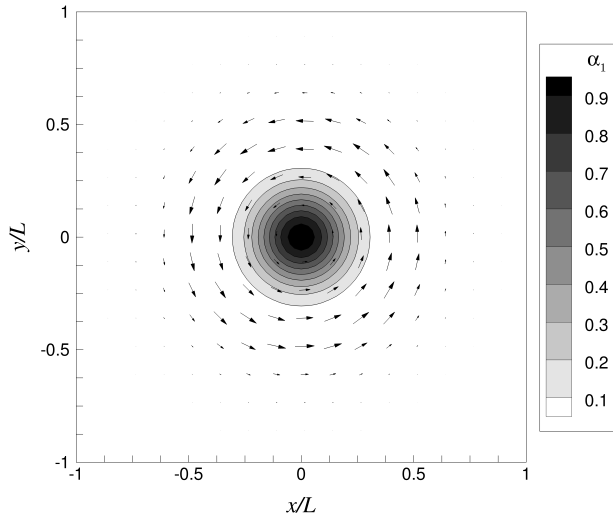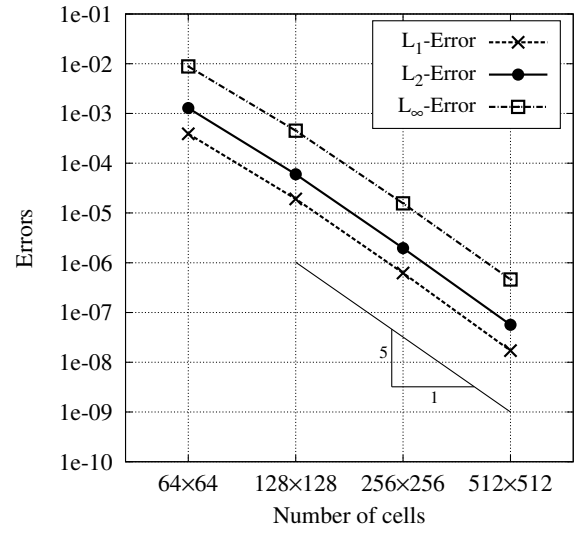
Figure 8: 2D multiphase vortex advection test-case: (a) initial configuration in the moving frame; (b) convergence order.
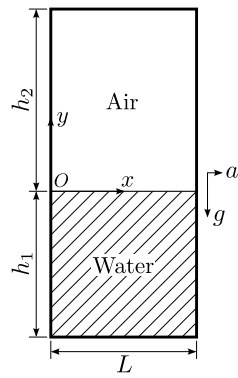

Figure 9: Initial configuration of the linear sloshing test-case.

Table 3: Geometrical and physical parameters of the linear sloshing test-case.

Parameter	Value
Tank width (L)	1 m
Initial water height (h_1)	1 m
Initial air height (h_2)	1.25 m
Gravity (g)	9.81 m/s^2
Horizontal acceleration (a)	0.01g
Speed of sound in water (c_1)	100 m/s
Speed of sound in air (c_2)	100 m/s

Based on the linearized potential flow theory, the analytical solution of the interface elevation $\eta(x,t)$ is given as [6, 16]

$$\eta(x,t) = \frac{a}{g}\left(x - \frac{L}{2} + \sum_{n=0}^{+\infty} \frac{4}{L\kappa_{2n+1}^2} \cos(\omega_{2n+1}t)\cos(\kappa_{2n+1}x) \right), \tag{66}$$

where

$$\begin{cases} \kappa_n = \dfrac{n\pi}{L}, \\ \omega_n = \sqrt{\dfrac{g\kappa_n(\rho_{1,0}-\rho_{2,0})}{\rho_{1,0}\coth(\kappa_n h_1)+\rho_{2,0}\coth(\kappa_n h_2)}}. \end{cases} \tag{67}$$

Figure 10 shows the time histories of the air-water interface elevation on the left and right walls of the tank, which are obtained using three uniform meshes of size $64\Delta x \times 144\Delta y$, $128\Delta x \times 288\Delta y$ and $256\Delta x \times 576\Delta y$. In addition, the shapes of the air-water interface, plotted by means of the contour line of $\alpha_1 = 0.5$ at four instants $t = 1$ s, 2 s, 3 s and 4 s, are provided in Figure 11. A good agreement can be observed between the present numerical result and the analytical solution, which shows the capacity of the proposed two-phase FV-WENO scheme to simulate accurately free-surface flows of high density ratio in such type of linear sloshing cases with small wave amplitude.

7.4. Wave propagation

The objective of the following test-case is to assess the capability of the present weakly-compressible two-phase finite volume scheme for handling long-period wave propagations near the free-surface (air-water interface), which is a challenging task for most either incompressible or compressible two-phase CFD methods due to the numerical diffusion effects introduced by the numerical schemes.

The configuration of this test-case is shown in Figure 12 and the parameters are given in Table 4. We consider the wave propagation in a 2D channel of infinite length. Periodic boundary conditions are applied on
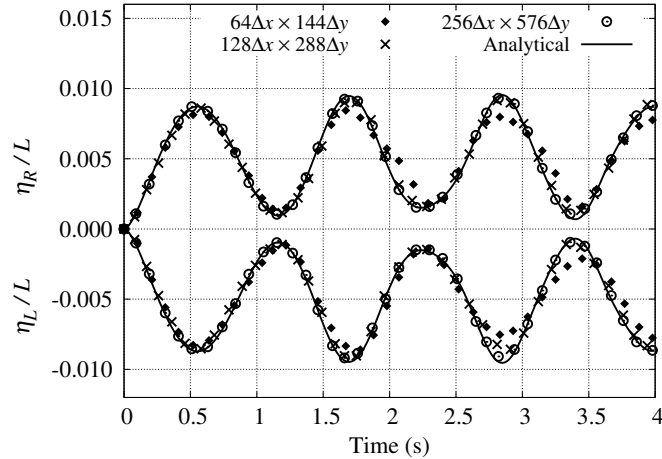
Figure 10: Time history of the interface elevations $\eta_L = \eta(0, t)$ and $\eta_R = \eta(L, t)$ on the left and right walls in the linear sloshing test-case with three mesh resolutions: $64\Delta x \times 144\Delta y$, $128\Delta x \times 288\Delta y$ and $256\Delta x \times 576\Delta y$.

the left and right hand sides of the computational domain. Free-slip boundary conditions are imposed on the upper and lower solid walls of the channel. Based on the parameters given in Table 4, the analytical solution can be obtained using the non-linear potential flow theory [10, 27], which is given as

$$
\begin{cases}
\eta(x, t) = \dfrac{a_0}{2} + \displaystyle\sum_{n=1}^{+\infty} a_n \cos\left(\kappa_n(x - c_p t)\right), \\[4mm]
\Phi(x, y, t) = b_0(x - c_p t) + \displaystyle\sum_{n=1}^{+\infty} b_n \dfrac{\cosh\left(\kappa_n(y + h)\right)}{\cosh(\kappa_n h)} \sin\left(\kappa_n(x - c_p t)\right),
\end{cases}
\tag{68}
$$

where η and Φ denote respectively the free-surface elevation and the potential function, the wave number $\kappa_n = 2\pi n/\lambda$ and the phase velocity $c_p = \lambda/T$ with $T \simeq 0.7018$ s being the wave propagation period obtained from the non-linear potential flow theory. Once the coefficients a_n and b_n are determined, the velocity and pressure fields can then be obtained as

$$
\begin{cases}
u(x, y, t) = \dfrac{\partial \Phi(x, y, t)}{\partial x}, \\[3mm]
v(x, y, t) = \dfrac{\partial \Phi(x, y, t)}{\partial y}, \\[3mm]
\dfrac{p(x, y, t)}{\rho_{1,0}} = R - gy - \dfrac{1}{2}c_p^2 - \dfrac{\partial \Phi(x, y, t)}{\partial t} - \dfrac{u^2(x, y, t) + v^2(x, y, t)}{2},
\end{cases}
\tag{69}
$$

where R is the Bernoulli constant.

The initial state in the water is imposed by means of Equation (69) with $t = 0$. However, since there is no analytical solution available in the air, in the present work, we choose to adopt a simple strategy in which both the pressure and velocity fields are initially equal to zero in the air. Due to the high density ratio
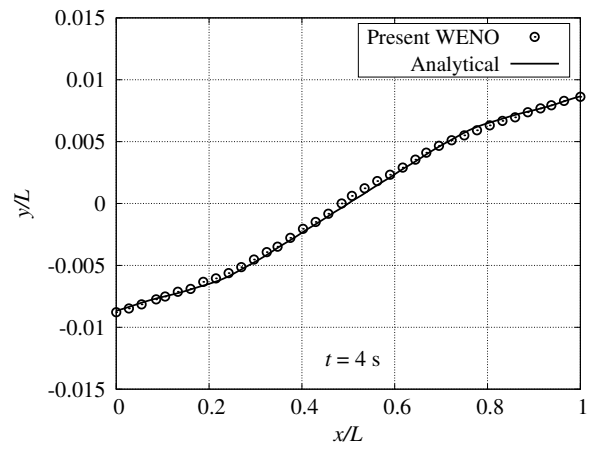
28
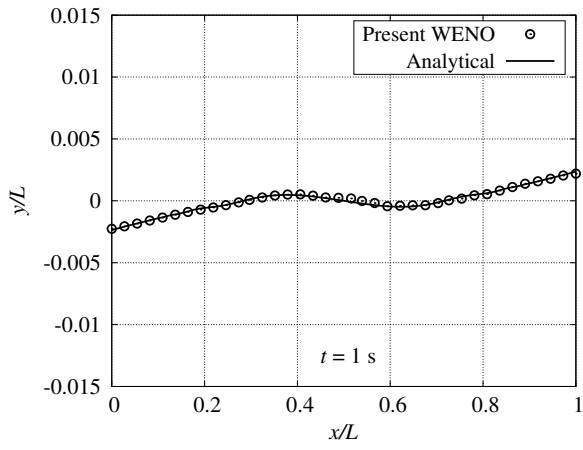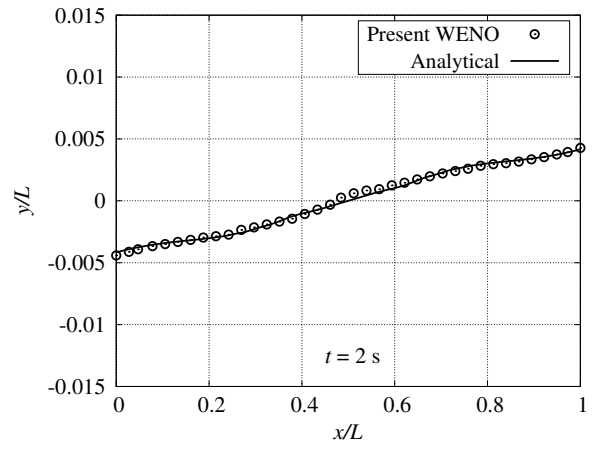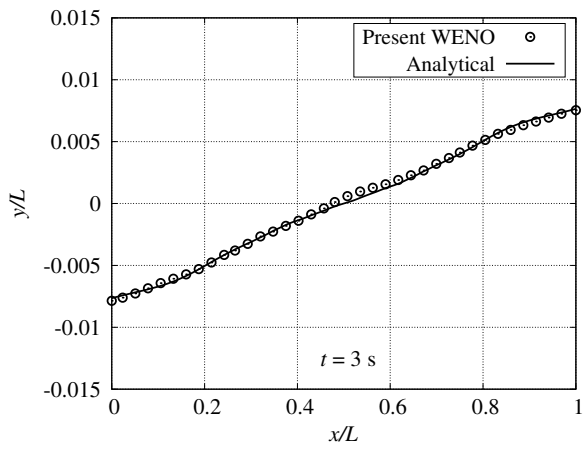
Figure 11: Shape of the air-water interface in the linear sloshing test-case using the mesh resolution $256\Delta x \times 576\Delta y$ at four instants: (a) $t = 1$ s; (b) $t = 2$ s; (c) $t = 3$ s; (d) $t = 4$ s.
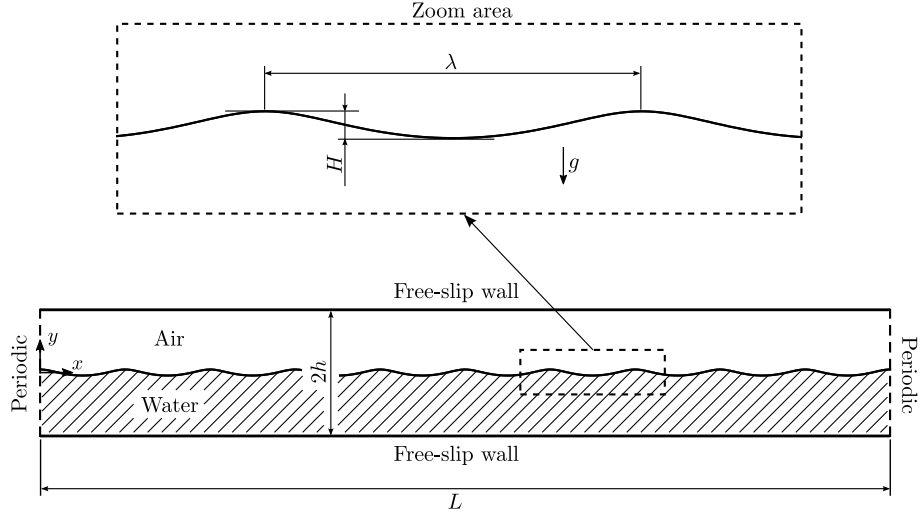
Figure 12: Configuration of the wave propagation test-case.

Table 4: Geometrical and physical parameters of the wave propagation test-case.

Parameter	Value
Length of the computational domain (L)	8.082 m
Water depth (h)	0.6 m
Height of the channel	$2h$
Wave length (λ)	$0.1L$
Wave height (H)	0.0576 m
Gravity (g)	9.81 m/s^2
Speed of sound in water (c_1)	30 m/s
Speed of sound in air (c_2)	30 m/s

$(\rho_{1,0}/\rho_{2,0} = 1000)$ between water and air, the numerical solution in the water is expected not to be significantly affected by this choice of initial condition.

The computational domain is discretized with a uniform mesh of size $1024\Delta x \times 512\Delta y$. This spatial resolution leads to $\lambda = 102.4\Delta x$ and $H = 24.576\Delta y$ with $\Delta x/\Delta y = 3.3675$. The total physical simulation time is set as $40T$, which is sufficiently long to assess the numerical diffusion. In the present work, this test-case has been carried out using the proposed WENO scheme and the 2nd-order accurate MUSCL [39] scheme with the 'minmod' slope-limiter. Both of the two numerical results are compared with the analytical solution obtained with the non-linear potential flow theory.

Figure 13 shows the shapes of the free-surface at each 10 periods $(10T)$, which are drawn using the contour line of $\alpha_1 = 0.5$. In this comparison, one may observe that the present WENO scheme almost retains the wave amplitude even after 40 periods $(40T)$, although the shape of the free-surface is slightly shifted, comparing to the analytical solution. Whereas in the result obtained with the MUSCL scheme, the wave amplitude is significantly damped and a large phase error can also be observed.

As for the computational cost, it is found that the numerical computation using the present WENO scheme is approximately 9.3 times slower than the one with the MUSCL scheme. In order to have a meaningful and fair comparison between the present WENO and MUSCL schemes, we carry out another simulation using the MUSCL scheme with a refined mesh (Mesh2: $2048\Delta x \times 1024\Delta y$), which costs almost the same as the present WENO scheme with the previous coarser mesh (Mesh1: $1024\Delta x \times 512\Delta y$). More precisely, in these conditions the WENO scheme is just 1.079 times slower than the MUSCL one. Figure 14 gives the numerical result of the MUSCL scheme using the refined mesh, which is compared with the previous ones. One may observe that the MUSCL scheme with the refined mesh still introduces more numerical diffusion than the proposed WENO scheme. This difference is clearly shown in Figure 15, where a fast Fourier transform with a moving window of size T has been carried out on the free-surface elevation $\eta_m(t) = \eta(L/2, t)$ in the middle of the domain. By comparing the first two harmonic amplitudes, it can be easily observed that the present WENO scheme is less diffusive and provides more accurate result.

In this specific test-case involving long-time wave propagation, the present 5th-order WENO scheme provides promising results in good agreement with the analytical solution and appears to be superior to the adopted 2nd-order MUSCL scheme. Nevertheless, it is worth noting that MUSCL schemes are often more robust in the presence of strong discontinuities such as shock waves.
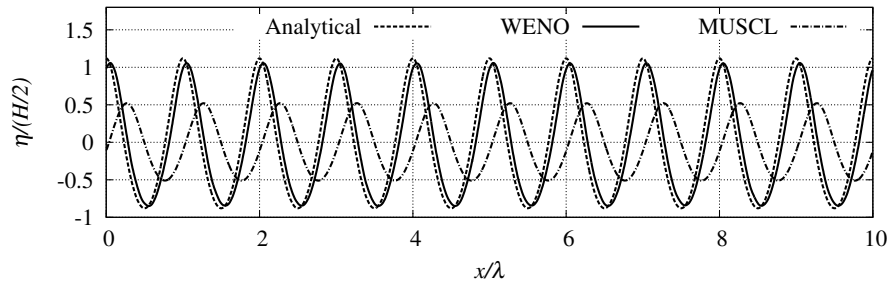
7.5. Dam-break flow

At last, we tried to apply the proposed weakly-compressible two-phase finite volume scheme to simulate a 2D dam-break flow involving moderately more violent impacts and higher dynamics than the previous test-cases.
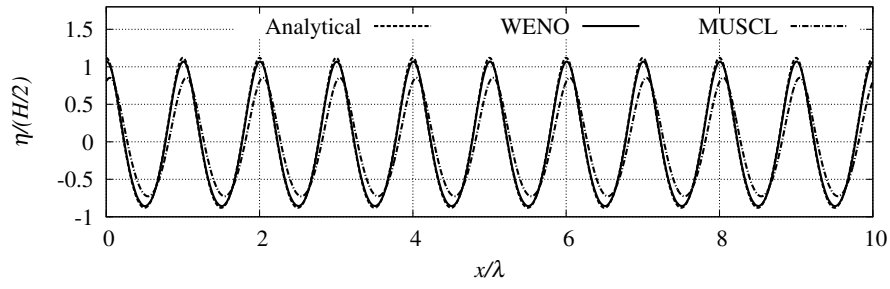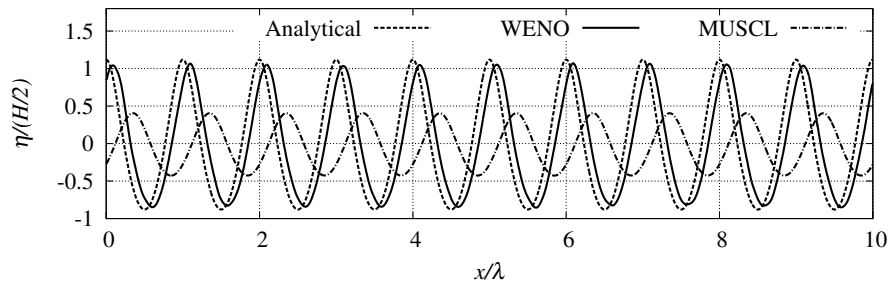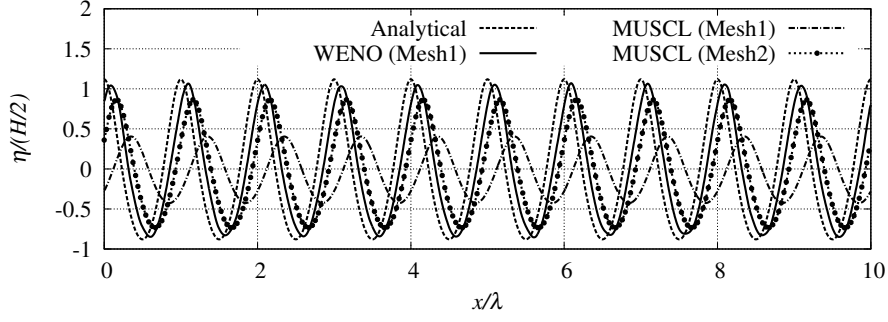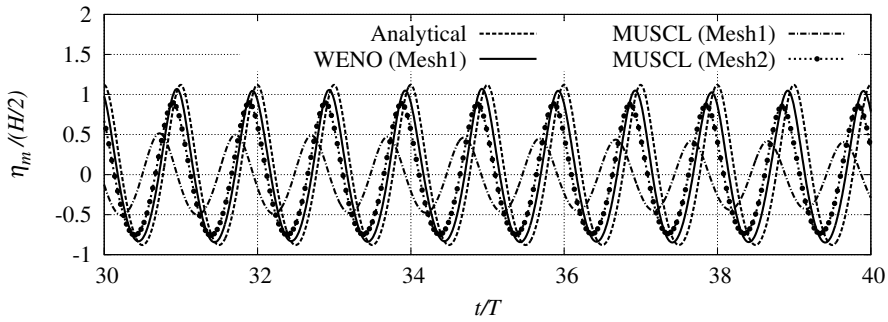
(a)
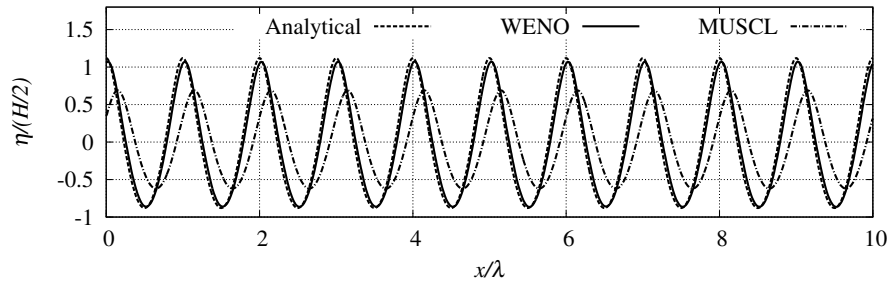
(b)

(c)

(d)

Figure 13: Shape of the free-surface in the wave propagation test-case using the proposed WENO scheme and the MUSCL scheme with the same mesh of resolution $1024\Delta x \times 512\Delta y$ at four instants: (a) $t = 10T$; (b) $t = 20T$; (c) $t = 30T$; (d) $t = 40T$.
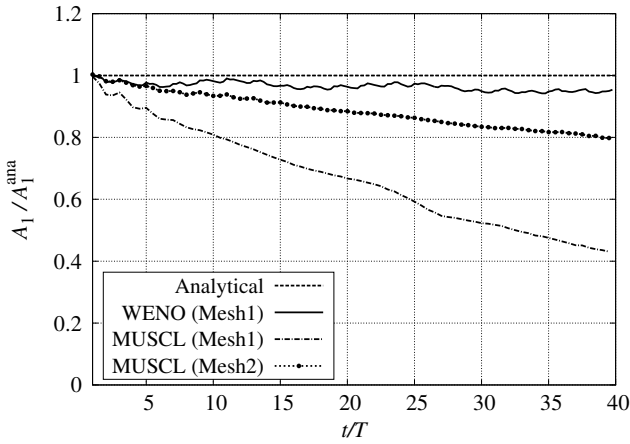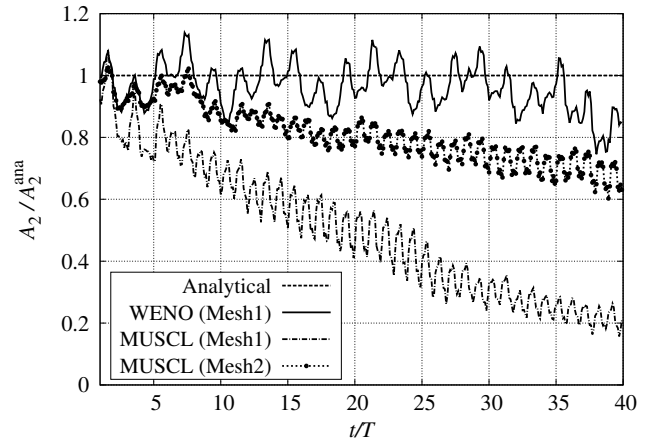
32

(a)

(b)

Figure 14: Numerical result obtained with the MUSCL scheme using the refined mesh (Mesh2: $2048\Delta x \times 1024\Delta y$): (a) shape of the free-surface at $t = 40T$; (b) time evolution of the free-surface elevation $\eta_m(t) = \eta(L/2, t)$ during the last 10 wave periods.

(a)

(b)

Figure 15: Moving-window fast Fourier transform of the free-surface elevation $\eta_m(t) = \eta(L/2, t)$: (a) 1$^{\text{st}}$-harmonic amplitude A_1/A_1^{ana} with $A_1^{\text{ana}} \simeq 2.8166 \times 10^{-2}$ m; (b) 2$^{\text{nd}}$-harmonic amplitude A_2/A_2^{ana} with $A_2^{\text{ana}} \simeq 3.3283 \times 10^{-3}$ m.

33

Figure 16 shows the initial configuration of this test-case and the computational parameters are given in Table 5.
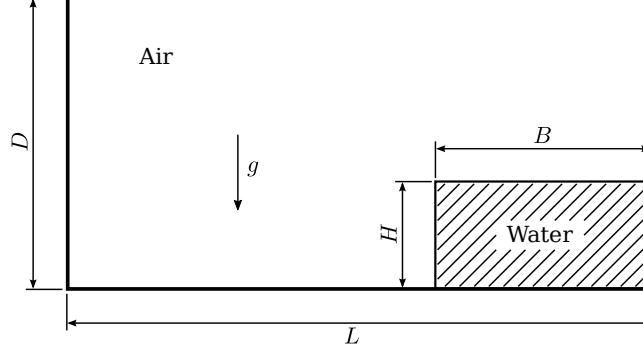

Figure 16: Initial configuration of the dam-break flow test-case.

Table 5: Geometrical and physical parameters of the dam-break flow test-case.

Parameter	Value
Length of the tank (L)	1.61 m
Height of the tank (D)	$0.5L$
Width of the water column (B)	0.6 m
Height of the water column (H)	0.3 m
Gravity (g)	9.81 m/s^2
Speed of sound in water (c_1)	100 m/s
Speed of sound in air (c_2)	100 m/s

Initially, a column of water at rest under the gravity is located at the right lower corner of a closed tank which is composed of four free-slip walls. The fluid domain is discretized with a uniform mesh of size $256\Delta x \times 128\Delta y$. Figure 17 shows the volume fraction field α_1 of water at three instants, which are compared with the experimental measurements obtained by Lobovsky et al. [23]. As time evolves, the water column falls down under the gravity effect and then impacts on the opposite solid wall. In addition, the water front position and the pressure signal at the left lower corner (Sensor 1 in [23]) are shown in Figure 18. From these comparisons between the present numerical results and the experimental measurements, one may observe that the proposed scheme provides reasonably accurate results in good agreement with the experimental ones. Nevertheless, some pressure oscillations can be found, as shown in Figure 18-(b), for the pressure sensor at the left lower corner of the tank. This pressure oscillation is due to the fact that only one stencil (even not smooth) is available for the WENO reconstruction at this corner where huge gradients can be present, especially when the water front impacts

34

on the vertical solid wall. Improving the numerical stability of the present scheme near solid walls is of great importance and will be considered in future works.
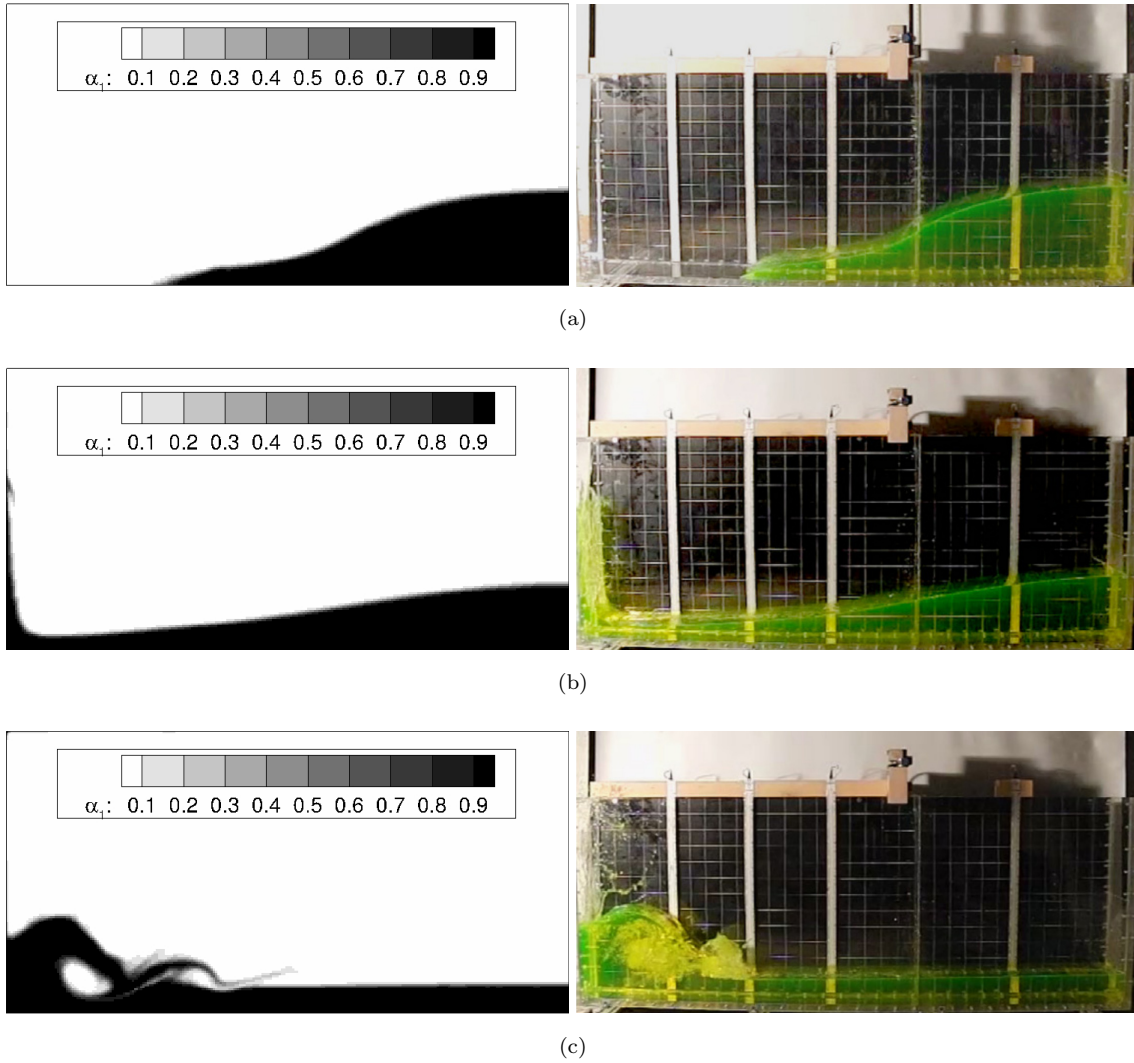

(a)

(b)

(c)

Figure 17: Comparison of flow patterns between the numerical results (left) obtained with the proposed WENO scheme and the experimental measurements (right) carried out by Lobovsky et al. [23] (reprinted with permission from Elsevier) at three dimensionless instants $t^* = t\sqrt{g/H}$: (a) $t^* \simeq 1.58$; (b) $t^* \simeq 3.27$; (c) $t^* \simeq 6.67$.

8. Conclusions

In the present paper, a finite volume WENO scheme is proposed for simulating weakly-compressible two-phase flows. Based on a three-equation hyperbolic system of equations, the semi-discrete equations in the present
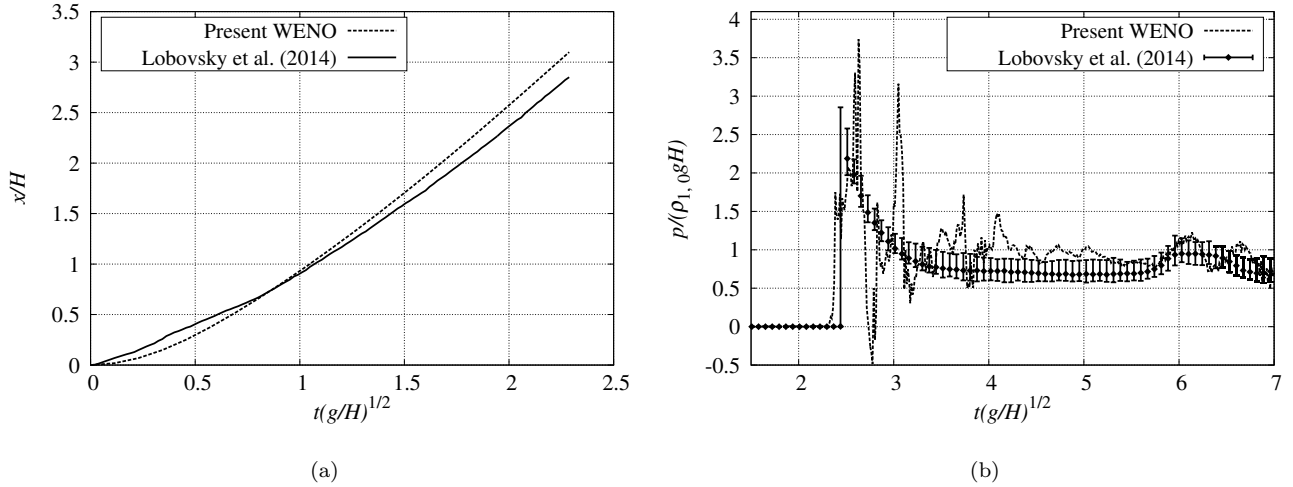
Figure 18: Water front position and pressure signal in the dam-break flow test-case: (a) time history of the water front position; (b) pressure signal at the left lower corner of the tank.

method are explicitly integrated in time using the Runge-Kutta scheme. A modified WENO reconstruction scheme is proposed, which consists in using a common smoothness indicator for $\tilde{\rho}_1$ and $\tilde{\rho}_2$ and reconstructing the mixture's density ρ for obtaining the velocity at cell-interfaces. In addition, based on the linearization of the generalized Riemann invariants, an approximate two-phase Riemann flux solver is proposed to compute the numerical flux at cell-interfaces. It is then shown that the proposed method can retain the formal convergence order of WENO scheme in multi-dimensional cases and avoid strictly pressure oscillations in the Abgrall test-case. In the numerical examples of free-surface flows such as the linear sloshing and the wave propagation test-cases, it is observed that the proposed scheme introduces a very small numerical diffusion and predicts correctly the behaviors of free-surface waves even during a long-time simulation. In the dam-break flow test-case, the present FV-WENO scheme provides a numerical result in good agreement with the experimental data. Some pressure oscillations occur at the corner of the tank, due to the fact that only one stencil is available at this place for the WENO reconstruction. In the future work, viscous and surface tension terms will be considered for more complex two-phase flows.

References

[1] R. Abgrall. How to prevent pressure oscillations in multicomponent flow calculations: a quasi conservative approach. *Journal of Computational Physics*, 125:150–160, 1996.

[2] R. Abgrall and S. Karni. Computations of compressible multifluids. *Journal of Computational Physics*, 169:594–623, 2001.

[3] M.R. Baer and J.W. Nunziato. A two-phase mixture theory for the Deflagration-to-Detonation Transition (ddt) in reactive granular materials. *International Journal of Multiphase Flow*, 12:861–889, 1986.

[4] P. Batten, N. Clarke, C. Lambert, and D.M. Causon. On the choice of wavespeeds for the HLLC Riemann solver. *SIAM Journal on Scientific Computing*, 18:1553–1570, 1997.

[5] P. Bigay, G. Oger, P.M. Guilcher, and D. Le Touzé. A weakly-compressible cartesian grid approach for hydrodynamic flows. *Computer Physics Communications*, 220:31–43, 2017.

[6] G. Chanteperdrix. *Modélisation et simulation numérique d'écoulements diphasiques à interface libre. Application à l'étude des mouvements de liquides dans les résservoirs de véhicules spatiaux.* PhD thesis, L'École Nationale Supérieure de l'Aéronautique et de l'Espace, 2004.

[7] V. Coralic and T. Colonius. Finite-volume WENO scheme for viscous compressible multicomponent flows. *Journal of Computational Physics*, 274:95–121, 2014.

[8] G. Costigan and P.B. Whalley. Measurements of the speed of sound in air-water flows. *Chemical Engineering Journal*, 66:131–135, 1997.

[9] D.A. Drew. Mathematical modelling of two-phase flow. *Annual Review of Fluid Mechanics*, 15:261–291, 1983.

[10] G. Ducrozet, B. Bouscasse, M. Gouin, P. Ferrant, and F. Bonnefoy. CN-Stream: Open-source library for nonlinear regular waves using stream function theory. *arXiv:1901.10577*, 2019.

[11] M. Dumbser, A. Hidalgo, M. Castro, C. Parés, and E.F. Toro. FORCE schemes on unstructured meshes II: Non-conservative hyperbolic systems. *Computer Methods in Applied Mechanics and Engineering*, 199:625–647, 2010.

[12] M. Dumbser, A. Hidalgo, and O. Zanotti. High order space-time adaptive ADER-WENO finite volume schemes for non-conservative hyperbolic systems. *Computer Methods in Applied Mechanics and Engineering*, 268:359–387, 2014.

[13] P. Embid and M. Baer. Mathematical analysis of a two-phase continuum mixture theory. *Continuum Mechanics and Thermodynamics*, 4:279–312, 1992.

[14] R.P. Fedkiw, B. Merriman, and S. Osher. Simplified discretization of systems of hyperbolic conservation laws containing advection equations. *Journal of Computational Physics*, 157:302–326, 2000.

[15] E. Franquet and V. Perrier. RungeKutta discontinuous Galerkin method for the approximation of Baer and Nunziato type multiphase models. *Journal of Computational Physics*, 231:4096–4141, 2012.

[16] N. Grenier, J.P. Vila, and P. Villedieu. An accurate low-Mach scheme for a compressible two-fluid model applied to free-surface flows. *Journal of Computational Physics*, 252:1–19, 2013.

[17] L.H. Han, X.Y. Hu, and N.A. Adams. Adaptive multi-resolution method for compressible multi-phase flows with sharp interface model and pyramid data structure. *Journal of Computational Physics*, 262:131–152, 2014.

[18] G.S. Jiang and C.-W. Shu. Efficient implementation of weighted ENO schemes. *Journal of Computational Physics*, 126:202–228, 1996.

[19] E. Johnsen and T. Colonius. Implementation of WENO schemes in compressible multicomponent flow problems. *Journal of Computational Physics*, 219:715–732, 2006.

[20] P.D. Lax. Hyperbolic systems of conservation laws II. *Communications on Pure and Applied Mathematics*, 10:537–566, 1957.

[21] S. Le Martelot, R. Saurel, and B. Nkonga. Towards the direct numerical simulation of nucleate boiling flows. *International Journal of Multiphase Flow*, 66:62–78, 2014.

[22] X.D. Liu, S. Osher, and T. Chan. Weighted essentially non-oscillatory schemes. *Journal Computational Physics*, 115:200–212, 1994.

[23] L. Lobovský, E. Botia-Vera, F. Castellana, J. Mas-Soler, and A. Souto-Iglesias. Experimental investigation of dynamic pressure loads during dam break. *Journal of Fluids and Structures*, 48:407–434, 2014.

[24] A. Murrone and H. Guillard. A five equation reduced model for compressible two phase flow problems. *Journal of Computational Physics*, 202:664–698, 2005.

[25] B. Perthame and C.-W. Shu. On positivity preserving finite volume schemes for Euler equations. *Numerische Mathematik*, 73:119–130, 1996.

[26] V.H. Ransom and D. L. Hicks. Hyperbolic two-pressure models for two-phase flow. *Journal of Computational Physics*, 53:124–151, 1984.

[27] M.M. Rienecker and J.D. Fenton. A Fourier approximation method for steady water waves. *Journal of Fluid Mechanics*, 104:119–137, 1981.

[28] M. Rodriguez and E. Johnsen. A high-order accurate five-equations compressible multiphase approach for viscoelastic fluids and solids with relaxation and elasticity. *Journal of Computational Physics*, 379:70–90, 2019.

[29] R. Saurel, P. Boivin, and O. Le Métayer. A general formulation for cavitating, boiling and evaporating flows. *Computers and Fluids*, 128:53–64, 2016.

[30] C.-W. Shu. Essentially non-oscillatory and weighted essentially non-oscillatory schemes for hyperbolic conservation laws. In *Advanced Numerical Approximation of Nonlinear Hyperbolic Equations: Lectures given at the 2nd Session of the Centro Internazionale Matematico Estivo (C.I.M.E.) held in Cetraro, Italy, June 23–28, 1997*, pages 325–432. Springer Berlin Heidelberg, 1998.

[31] C.-W. Shu. High order WENO and DG methods for time-dependent convection-dominated PDEs: A brief survey of several recent developments. *Journal of Computational Physics*, 316:598–613, 2016.

[32] R.K. Shukla, C. Pantano, and J.B. Freund. An interface capturing method for the simulation of multi-phase compressible flows. *Journal of Computational Physics*, 229:7411–7439, 2010.

[33] H.B. Stewart and B. Wendroff. Two-Phase Flow: Models and Methods. *Journal of Computational Physics*, 56:363–409, 1984.

[34] V.A. Titarev and E.F. Toro. Finite-volume WENO scheme for three-dimensional conservation laws. *Journal of Computational Physics*, 201:238–260, 2004.

[35] S.A. Tokareva and E.F. Toro. HLLC-type Riemann solver for the Baer-Nunziato equations of compressible two-phase flow. *Journal of Computational Physics*, 229:3573–3604, 2010.

[36] S.A. Tokareva and E.F. Toro. A flux splitting method for the Baer-Nunziato equations of compressible two-phase flow. *Journal of Computational Physics*, 323:45–74, 2016.

[37] E.F. Toro. *Riemann Solvers and Numerical Methods for Fluid Dynamics*. Springer, 2009.

[38] E.F. Toro, M. Spruce, and W. Speares. Restoration of the contact surface in the HLL-Riemann solver. *Shock Waves*, 4:25–34, 1994.

[39] B. van Leer. Towards the ultimate conservative difference scheme. V. A second-order sequel to Godunov's method. *Journal of Computational Physics*, 32:101–136, 1979.

[40] L. Vittoz, G. Oger, M. de Leffe, and D. Le Touzé. Comparisons of weakly-compressible and truly incompressible approaches for viscous flow into a high-order Cartesian-grid finite volume framework. *Journal of Computational Physics: X*, 1:100015, 2019.

[41] B. Wang, G. Xiang, and X.Y. Hu. An incremental-stencil WENO reconstruction for simulation of compressible two-phase flows. *International Journal of Multiphase Flow*, 104:20–31, 2018.

[42] Z.J. Wang, K. Fidkowski, R. Abgrall, F. Bassi, D. Caraeni, A. Cary, H. Deconinck, R. Hartmann, K. Hillewaert, H.T. Huynh, N. Kroll, G. May, P.-O. Persson, B. van Leer, and M. Visbal. High-order CFD methods: current status and perspective. *International Journal for Numerical Methods in Fluids*, 72:811–845, 2013.

[43] X. Zhang and C.-W. Shu. On maximum-principle-satisfying high order schemes for scalar conservation laws. *Journal of Computational Physics*, 229:3091–3120, 2010.

[44] X. Zhang and C.-W. Shu. Positivity-preserving high order finite difference WENO schemes for compressible Euler equations. *Journal of Computational Physics*, 231:2245–2258, 2012.

Appendix A: Speed of sound in the two-phase mixture

The speed of sound of the mixture is given in Equation (42), or as

$$\rho c^2 = \tilde{\rho}_1 \tilde{c}_1^2 + \tilde{\rho}_2 \tilde{c}_2^2, \tag{A.1}$$

in which $\tilde{c}_1^2$ and $\tilde{c}_2^2$ are defined in Equation (39).

Using the instantaneous pressure equilibrium condition $p = p_1 = p_2$ and the barotropic EOS (2), one can have

$$\tilde{c}_1^2 = \frac{\partial p_1}{\partial \tilde{\rho}_1} = \frac{\partial p_1}{\partial \rho_1}\frac{\partial \rho_1}{\partial \tilde{\rho}_1} = c_1^2\left(\frac{1}{\alpha_1} - \frac{\rho_1}{\alpha_1}\frac{\partial \alpha_1}{\partial \tilde{\rho}_1}\right). \tag{A.2}$$

Meanwhile, the equality $p_1 = p_2$ gives

$$p_0 + c_1^2\left(\left(\frac{\tilde{\rho}_1}{\alpha_1}\right) - \rho_{1,0}\right) = p_0 + c_2^2\left(\left(\frac{\tilde{\rho}_2}{\alpha_2}\right) - \rho_{2,0}\right), \tag{A.3}$$

where α_1 (or $\alpha_2 = 1 - \alpha_1$) can be considered as a function of $\tilde{\rho}_1$ and $\tilde{\rho}_2$. Now, taking the partial derivative of Equation (A.3) with respect to $\tilde{\rho}_1$ yields

$$c_1^2 \frac{\alpha_1 - \tilde{\rho}_1 \dfrac{\partial \alpha_1}{\partial \tilde{\rho}_1}}{\alpha_1^2} = c_2^2 \frac{0 - \tilde{\rho}_2 \dfrac{\partial \alpha_2}{\partial \tilde{\rho}_1}}{\alpha_2^2}, \tag{A.4}$$

which gives

$$\frac{\partial \alpha_1}{\partial \tilde{\rho}_1} = \frac{\dfrac{c_1^2}{\alpha_1}}{\dfrac{\rho_1 c_1^2}{\alpha_1} + \dfrac{\rho_2 c_2^2}{\alpha_2}}. \tag{A.5}$$

Substituting Equation (A.5) into Equation (A.2) gives

$$\tilde{c}_1^2 = \frac{c_1^2}{\alpha_1} - \frac{\dfrac{\rho_1 c_1^4}{\alpha_1^2}}{\dfrac{\rho_1 c_1^2}{\alpha_1} + \dfrac{\rho_2 c_2^2}{\alpha_2}}. \tag{A.6}$$

Similarly, following the same procedure for the second phase $(k = 2)$, one can obtain

$$\tilde{c}_2^2 = \frac{c_2^2}{\alpha_2} - \frac{\dfrac{\rho_2 c_2^4}{\alpha_2^2}}{\dfrac{\rho_1 c_1^2}{\alpha_1} + \dfrac{\rho_2 c_2^2}{\alpha_2}}. \tag{A.7}$$

Finally, substituting Equation (A.6) and Equation (A.7) into Equation (A.1) gives

$$\rho c^2 = \frac{\rho_1 c_1^2 \rho_2 c_2^2}{\rho_1 c_1^2 \alpha_2 + \rho_2 c_2^2 \alpha_1}, \tag{A.8}$$

which can then be written as

$$\frac{1}{\rho c^2} = \frac{\alpha_1}{\rho_1 c_1^2} + \frac{\alpha_2}{\rho_2 c_2^2}, \tag{A.9}$$

from which one can easily find the speed of sound of the mixture Equation (3).

Appendix B: Analytical solution of the multiphase vortex advection test-case

Similar to the strategies proposed in [11, 15, 42], in the present work we derive firstly the steady analytical solution of the governing equations (1) with a cylindrical coordinate system, in which one has $x = r\cos\theta$, $y = r\sin\theta$ and $\mathbf{u} = u_\theta(r, \theta, t)\mathbf{e}_\theta + u_r(r, \theta, t)\mathbf{e}_r$ with u_θ and u_r being the velocity components in tangential and radial directions, respectively. By definition, one has $u_r(r, \theta, t) = 0$ and $\partial u_\theta / \partial\theta = 0$. It can then be easily verified that the two mass conservation equations are automatically satisfied. The momentum conservation equation for the two-phase mixture then becomes

$$\rho u_\theta^2 = r\frac{\partial p}{\partial r}. \tag{B.1}$$

By imposing

$$\begin{cases} \alpha_1(r, \theta, t) = (1 - 2\epsilon_\alpha)\exp\left(-\frac{r^2}{r_0^2}\right) + \epsilon_\alpha, \\[2ex] p(r, \theta, t) = P\left(1 - \exp\left(-\frac{r^2}{r_0^2}\right)\right), \end{cases} \tag{B.2}$$

41

where P, r_0 and ϵ_α are chosen as $P = 0.1\rho_{2,0}c_2^2$, $r_0 = 0.2L$ and $\epsilon_\alpha = 10^{-4}$ with $c_2 = 30$ m/s and $L = 1$ m.

With these two conditions, one can obtain the velocity field u_θ by solving Equation (B.1). The velocity components u and v in x- and y-directions of the Cartisian coordinate system is expressed as

$$
\begin{cases}
u(r, \theta, t) = -\sin\theta \sqrt{\dfrac{r}{\rho}\dfrac{\partial p}{\partial r}}, \\[2mm]
v(r, \theta, t) = +\cos\theta \sqrt{\dfrac{r}{\rho}\dfrac{\partial p}{\partial r}},
\end{cases}
\tag{B.3}
$$

which will be used as the initial velocity fields.

Finally, in order to have an unsteady test-case, we add two constants $U = 2$ m/s and $V = 2$ m/s to the previous velocity fields, so that this multiphase vortex is advected in the diagonal direction of the computational domain with a constant speed.

Acknowledgement